



Science Arts & Métiers (SAM)

is an open access repository that collects the work of Arts et Métiers Institute of Technology researchers and makes it freely available over the web where possible.

This is an author-deposited version published in: <https://sam.ensam.eu>
Handle ID: <http://hdl.handle.net/10985/14457>

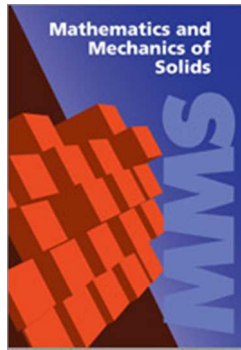
To cite this version :

Soheil FIROOZ, Saba SAEB, George CHATZIGEORGIOU, Fodil MERAGHNI, Paul STEINMANN, Ali JAVILI - A systematic study on homogenization and the utility of circular simplified RVE - Mathematics and Mechanics of Solids p.108128651882383 - 2019

Any correspondence concerning this service should be sent to the repository

Administrator : scienceouverte@ensam.eu





A systematic study on homogenization and the utility of circular simplified RVE

Journal:	<i>Mathematics and Mechanics of Solids</i>
Manuscript ID	MMS-18-0242
Manuscript Type:	Original Manuscript
Date Submitted by the Author:	07-Oct-2018
Complete List of Authors:	Firooz, Soheil Saeb, Saba Chatzigeorgiou, George; LEM3-UMR 7239 CNRS, Arts et Metiers ParisTech Metz-Lorraine, Meraghni, Fodil; LEM3-UMR 7239 CNRS, Arts et Metiers ParisTech Metz-Lorraine, MECHANICAL; Arts et Metiers ParisTech - Centre de Metz, Steinmann, Paul Javili, Ali; Bilkent Universitesi, MECHANICAL ENGINEERING DEPARTMENT
Keywords:	Hexagonal RVE, Composites, Homogenization, Hashin-Shtrikman bounds, CCA
Abstract:	Although both computational and analytical homogenization are well-established today, a thorough and systematic study to compare them is missing in the literature. This manuscript aims to provide an exhaustive comparison of the numerical computations and the analytical estimates such as Voigt, Reuss, Hashin-Shtrikman and composite cylinder assemblage (CCA). The numerical computations are associated with canonical boundary conditions imposed on either tetragonal RVE, hexagonal RVE or circular RVE using the finite element method. The circular RVE is employed to capture an effective isotropic material response suitable to be compared with the associated analytical estimates. The analytical results from CCA are in excellent agreement with the numerical results obtained from the circular RVE. We observe that the circular RVE renders identical responses for both linear displacement and periodic boundary conditions. In addition, the behavior of periodic and random micro-structures with different inclusion distributions are examined under various boundary conditions. Strikingly, for some specific micro-structures, the effective shear modulus does not lie within the Hashin-Shtrikman bounds. Finally, numerical simulations are carried out at finite

1
2
3
4
5
6
7
8
9
10
11
12
13
14
15
16
17
18
19
20
21
22
23
24
25
26
27
28
29
30
31
32
33
34
35
36
37
38
39
40
41
42
43
44
45
46
47
48
49
50
51
52
53
54
55
56
57
58
59
60

	deformations to compare different RVE types in the non-linear regime. Unlike other canonical boundary conditions, the uniform traction boundary conditions result in nearly identical effective responses for all types of the RVE indicating that it is less sensitive with respect to the underlying micro-structure. The numerical examples furnish adequate informations to serve as benchmarks.

SCHOLARONE™
Manuscripts

For Peer Review

A systematic study on homogenization and the utility of circular simplified RVE

Soheil Firooz^a, Saba Saeb^b, George Chatzigeorgiou^c, Fodil Meraghni^c, Paul Steinmann^{b,d}, Ali Javili^{a,*}

^aDepartment of Mechanical Engineering, Bilkent University, 06800 Ankara, Turkey

^bChair of Applied Mechanics, University of Erlangen-Nuremberg, Egerland Str. 5, 91058 Erlangen, Germany

^cLEM3-UMR 7239 CNRS, Arts et Metiers ParisTech Metz, 4 Rue Augustin Fresnel Metz 57078, France

^dSchool of Engineering, University of Glasgow, Glasgow G12 8QQ, United Kingdom

Abstract

Although both computational and analytical homogenization are well-established today, a thorough and systematic study to compare them is missing in the literature. This manuscript aims to provide an exhaustive comparison of the numerical computations and the analytical estimates such as Voigt, Reuss, Hashin–Shtrikman and composite cylinder assemblage (CCA). The numerical computations are associated with canonical boundary conditions imposed on either tetragonal RVE, hexagonal RVE or circular RVE using the finite element method. The circular RVE is employed to capture an effective *isotropic* material response suitable to be compared with the associated analytical estimates. The analytical results from CCA are in excellent agreement with the numerical results obtained from the circular RVE. We observe that the circular RVE renders identical responses for both linear displacement and periodic boundary conditions. In addition, the behavior of periodic and random micro-structures with different inclusion distributions are examined under various boundary conditions. Strikingly, for some specific micro-structures, the effective shear modulus does not lie within the Hashin–Shtrikman bounds. Finally, numerical simulations are carried out at finite deformations to compare different RVE types in the non-linear regime. Unlike other canonical boundary conditions, the uniform traction boundary conditions result in nearly identical effective responses for all types of the RVE indicating that it is less sensitive with respect to the underlying micro-structure. The numerical examples furnish adequate informations to serve as benchmarks.

Keywords: Homogenization, Hexagonal RVE, Circular RVE, Hashin–Shtrikman bounds, CCA, Composites

1. Introduction

Heterogeneous materials possess more complex behavior compared to their associated constituents. Therefore, composites have been the subject of an increasing interest in many engineering applications in the past decades. The

*Corresponding author.

Email addresses: soheil.firooz@bilkent.edu.tr (Soheil Firooz), saba.saeb@ltm.uni-erlangen.de (Saba Saeb), georges.chatzigeorgiou@ensam.eu (George Chatzigeorgiou), fodil.meraghni@ensam.eu (Fodil Meraghni), paul.steinmann@ltm.uni-erlangen.de (Paul Steinmann), ajavili@bilkent.edu.tr (Ali Javili)

mechanical behavior of heterogeneous materials is highly dependent on their micro-structural characteristics. Conducting experiments on numerous materials with various phases is not practical. Also, performing a numerical simulation on the whole macro-structure would include a huge number of variables which is extremely complicated, if not impossible. As a result, micro-mechanically based determination of the overall response of composites is of great significance.

Multi-scale methods have been developed to determine the overall response of heterogeneous media in terms of the constitutive behavior of their underlying microstructures. Multi-scale methods are categorized into concurrent methods and homogenization methods. In the concurrent methods [1–4], the problems at the microscopic and macroscopic scales are solved simultaneously, which requires a strong coupling between the two scales. In the homogenization method [5–15], the micro-problem and macro-problem are solved separately. Homogenization pioneered by Hill [16, 17] and Ogden [18] relies on (i) the assumption of the separation of the length scale between the micro- and macro-problem and (ii) the energy equivalence between the two scales known as the Hill–Mandel condition [16, 19]. Furthermore, the homogenization methods fall into analytical homogenization and computational homogenization. Pioneering contributions in analytical homogenization include [20–29] and later extended in [30–38]. See [39] for some comparisons of analytical and computational approaches of micro-mechanics. Despite providing useful information, the analytical homogenization approach requires certain simplifications on the microstructure such as its geometry and distribution pattern. On the contrary, the computational homogenization method is capable of dealing with such complexities, thus it has been widely adopted in the past decades, see [40–55] among others. For detailed reviews on computational homogenization, see [56–58]. Computational homogenization is essentially based on calculating the macroscopic quantities from the solution of a boundary value problem at the micro-scale. Recently, a number of methods have been developed to reduce the computational cost and increase the accuracy of multi-scale analysis [59–63].

The average-field theory [64, 65] is employed in order to bridge the microscopic quantities to their macroscopic counterparts. This theory relates the properties of continua at the macro-scale to the volume averages of their counterparts at the micro-scale. In doing so, the boundary conditions at the micro-scale are chosen such that the Hill–Mandel condition is satisfied. A broader group of admissible boundary conditions to fill the gap between the homogeneous boundary conditions was derived in [66]. The computational implementation algorithms of DBC and PBC are discussed in [67, 68]. The effects of various boundary conditions on the overall behavior of periodic unidirectional linear composites has been investigated in [69]. Furthermore, [70–72] proposed a mixed-type boundary condition composed of linear displacement boundary conditions and constant traction boundary conditions to obtain an elasticity tensor that lies between the elasticity tensors obtained from homogeneous boundary conditions. For further details on the

Table 1: Definitions of frequently used abbreviations and notations

DBC :	displacement boundary condition	$M\{\bullet\}$:	macroscopic $\{\bullet\}$	\mathcal{B} :	body of the domain
PBC :	periodic boundary condition	$\{\bullet\}_N$:	Neumann part of $\{\bullet\}$	$\partial\mathcal{B}$:	boundary of the domain
TBC :	traction boundary condition	$\{\bullet\}_D$:	Dirichlet part of $\{\bullet\}$	\boldsymbol{F} :	deformation gradient
CCA :	composite cylinder assemblage	$\{\bullet\}_0$:	$\{\bullet\}$ at material configuration	$\boldsymbol{\varphi}$:	nonlinear deformation map
HSB :	Hashin–Shtrikman bounds	$\{\bullet\}_I$:	$\{\bullet\}$ at spatial configuration	\boldsymbol{N} :	unit normal vector
f :	volume fraction	ν :	Poisson ratio	\boldsymbol{t} :	traction vector
SR :	stiffness ratio	κ :	bulk modulus	ψ :	free energy density
RVE :	representative volume element	λ :	first Lamé parameter	\boldsymbol{P} :	Piola stress
$\{\bullet\}^P$:	prescribed $\{\bullet\}$	μ :	second Lamé parameter	\mathbb{A} :	Piola tangent

formulation, implementation and application of appropriate boundary conditions in the context of the computational homogenization, see [73–79].

To establish a computational homogenization framework, it is essential to identify a representative volume element (RVE). A proper RVE must be selected such that it contains enough details to sufficiently represent the microstructure of the material and it has to be small enough to be considered as a microstructure surrounded by copies similar to itself, so as to fulfill the assumption of scale separation. In most cases, a proper RVE for a random microstructure is regarded as the smallest possible structure which could sufficiently capture the macroscopic response of the macro-structure. For more details on the definition of the RVE, see [80–85] among others. Although small, the RVE could still be too complex for computational homogenization. Thus, instead of studying a complex RVE, one could construct a simpler, however statistically similar RVE also referred to as SSRVE, see [86, 87]. Here, the term RVE indicates a simplified micro-structure in the sense of SSRVE [86, 87] or SRVE [88]. In this contribution, we present a systematic study on the computational and analytical homogenization by considering three types of RVEs; tetragonal, hexagonal and circular RVE, shown in Fig. 1. Note that the cutout of a real micro-structure with random distribution of particles can eventually result in isotropic effective behavior. While tetragonal and hexagonal packings are space-filling, only the circular RVE can furnish isotropic effective behavior suitable for comparing with analytical solutions here and it is the only RVE that could reach the maximum volume fraction of a real cutout of a material.

Table 1 provides a list of definitions for frequently used abbreviations in this manuscript as well as symbols and notations used to describe the mathematical aspects of the problem. The rest of the manuscript is organized as follows. The theory including the governing equations at both scales, bridging between the scales and satisfying the Hill–Mandel condition via appropriate boundary conditions is presented in Section 2. Material modeling and analytical approaches are detailed in Section 3, followed by a thorough comparison of the numerical and analytical

1
2
3
4
5
6
7
8
9
10
11
12
13
14
15
16
17
18
19
20
21
22
23
24
25
26
27
28
29
30
31
32
33
34
35
36
37
38
39
40
41
42
43
44
45
46
47
48
49
50
51
52
53
54
55
56
57
58
59
60

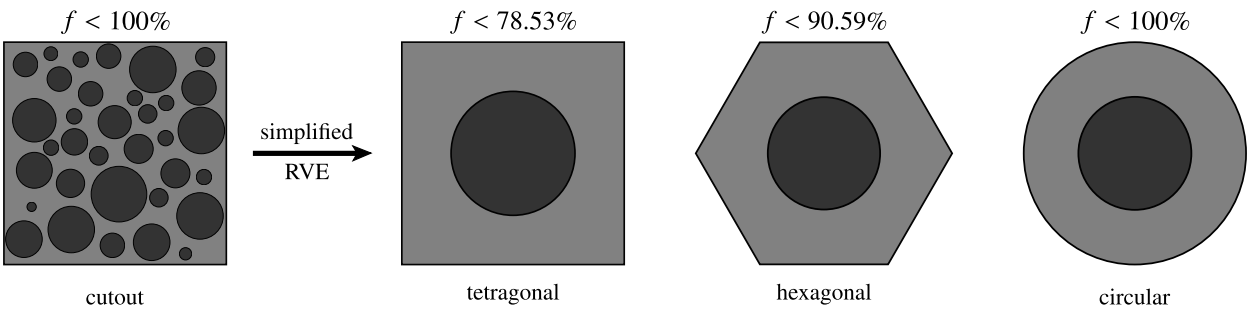


Figure 1: Complex RVE and its *simplified* counterparts. The inclusion volume fraction at the cutout could reach 100%. The cutout (left) shall be understood as the RVE. Three *simplified* RVEs are suggested to be sufficient to replace the cutout, namely tetragonal RVE, hexagonal RVE and circular RVE. For tetragonal RVE, the maximum reachable volume fraction is 78.53%. For hexagonal RVE this value is 90.59% and for circular RVE it could reach its maximum value, which is 100%. The cutout of the real micro-structure can eventually result in isotropic effective behavior. Both tetragonal and hexagonal packings are space-filling, hence intuitively are suitable candidates for a simplified RVE. However, only the circular RVE can furnish isotropic effective behavior resembling the real micro-structure. Furthermore, the circular RVE is the only simplified RVE that could reach the maximum volume fraction of a real cutout of the material.

methods to predict the effective response of heterogeneous materials. Section 4 extends the computational homogenization framework to finite deformations and the effects of RVE type and boundary condition are examined. Section 5 summarizes this work and provides further outlook.

2. Computational homogenization

This section elaborates on the theoretical aspects of computational homogenization and bridging the scales. The content of this section is fairly standard, however, in order to set the stage, the important aspects of computational homogenization are briefly reviewed. A detailed expositions on the formulation of computational homogenization and the associated numerical implementation can be found in [9, 56, 89–91] among others. Central to computational homogenization is the separation of the length scales between the micro- and the macro-scale. The key idea of computational homogenization is to identify the effective properties at the macro-scale through averaging of the micro-problem, see [92–98]. At the micro scale, it is assumed that the constitutive response of each phase is known. Solving the associated boundary value problem at the micro-scale and proper averaging over the RVE renders the overall response at the macro-scale. The micro-problem could be either strain-driven or stress-driven. In strain-driven homogenization, the macroscopic deformation gradient is prescribed and the macroscopic stress is calculated. On the contrary, the macroscopic stress is prescribed in stress-driven homogenization for an unknown macroscopic deformation gradient. This contribution is based on first-order strain-driven computational homogenization based on the deformation gradient and the Piola stress. In this section, the macro-problem is formulated first. This is then followed by the micro-problem definition. Finally, the micro-to-macro-transition and the Hill–Mandel condition are addressed afterwards.

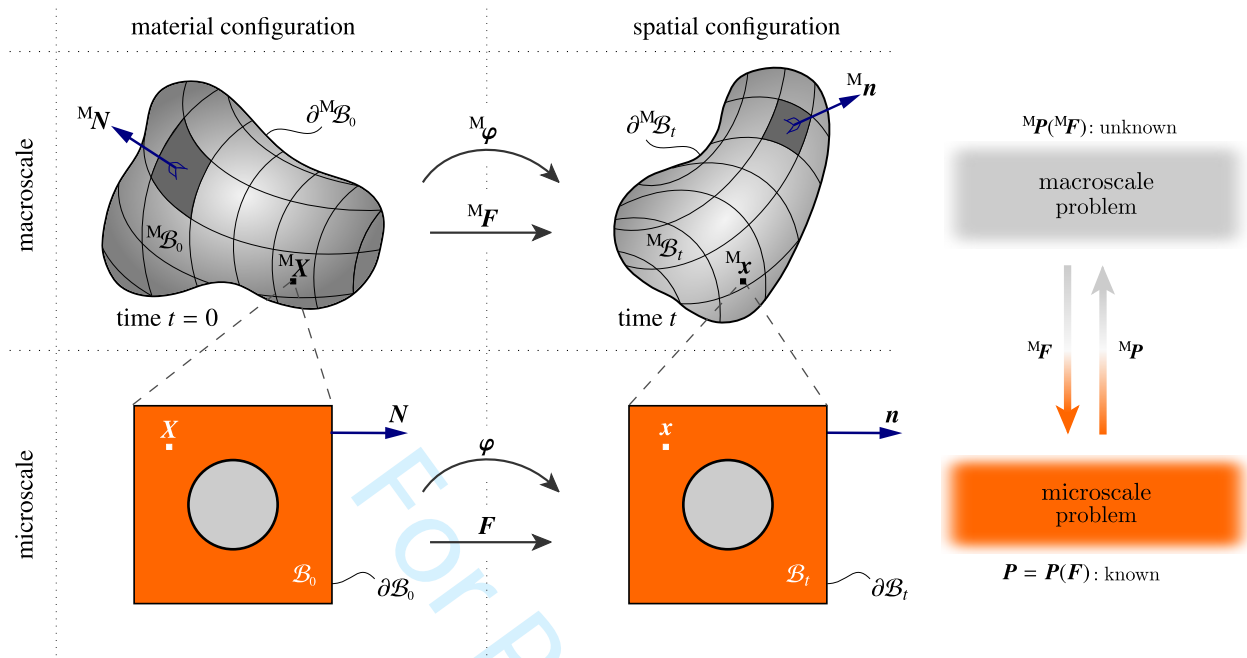


Figure 2: Computational homogenization graphical summary. The material configuration at the macro-scale ${}^M\mathcal{B}_0$ with the boundary of $\partial{}^M\mathcal{B}_0$ is mapped to its spatial counterpart ${}^M\mathcal{B}_t$ with the boundary of $\partial{}^M\mathcal{B}_t$. The non-linear map ${}^M\varphi$ maps points ${}^M\mathbf{X}$ from the material configuration to ${}^M\mathbf{x}$ in the spatial configuration. Line elements are mapped from the material configuration to the spatial configuration via ${}^M\mathbf{F}$. The domain \mathcal{B}_0 at the micro-scale corresponds to the RVE. In a strain-driven homogenization framework, the macroscopic deformation gradient is the input of the micro-problem and the macroscopic Piola stress is obtained by solving the boundary value problem at the micro-scale.

2.1. Macro-problem definition

Let a macroscopic continuum body take the material configuration ${}^M\mathcal{B}_0$ at time $t = 0$ and the spatial configuration ${}^M\mathcal{B}_t$ at time $t > 0$, as shown in Fig. 2. The boundaries of the body in the material and the spatial configuration are denoted as $\partial{}^M\mathcal{B}_0$ and $\partial{}^M\mathcal{B}_t$, respectively. Moreover, ${}^M\mathbf{N}$ and ${}^M\mathbf{n}$ define the material and spatial outward unit normal vectors to the boundaries. The material point ${}^M\mathbf{X}$ is mapped to its spatial counterpart ${}^M\mathbf{x}$ via the nonlinear deformation map ${}^M\varphi$ as ${}^M\mathbf{x} = {}^M\varphi({}^M\mathbf{X})$. The infinitesimal line element $d{}^M\mathbf{X}$ from the material configuration is mapped to $d{}^M\mathbf{x}$ in the spatial configuration via the linear map ${}^M\mathbf{F}$ as $d{}^M\mathbf{x} = {}^M\mathbf{F} \cdot d{}^M\mathbf{X}$ where ${}^M\mathbf{F} = {}^M\text{Grad}{}^M\varphi$ is the macroscopic deformation gradient. In addition, the Jacobian determinant ${}^MJ = \det{}^M\mathbf{F}$ maps the infinitesimal material volume element $d{}^MV$ to its spatial counterpart $d{}^Mv$ via $d{}^Mv = {}^MJ d{}^MV$. Finally, the normal map ${}^MJ{}^M\mathbf{F}^{-t}$ transforms the directional surface element from the material configuration $d{}^M\mathbf{S} = d{}^M\mathbf{S} {}^M\mathbf{N}$ to the directional surface element in the spatial configuration $d{}^M\mathbf{s} = d{}^M\mathbf{S} {}^M\mathbf{n}$ as $d{}^M\mathbf{s} = {}^MJ {}^M\mathbf{F}^{-t} \cdot d{}^M\mathbf{S}$. The governing equations for the macro-problem are the balances of linear and angular momentum. For a quasi-static case, the balance of linear momentum reads

$${}^M\text{Div}{}^M\mathbf{P} + {}^M\mathbf{b}_0^p = 0 \text{ in } {}^M\mathcal{B}_0, \quad {}^M\mathbf{P} \cdot {}^M\mathbf{N} = {}^M\mathbf{t}_0 \text{ on } \partial{}^M\mathcal{B}_0, \quad \text{with} \quad {}^M\mathbf{t}_0 = {}^M\mathbf{t}_0^p \text{ on } \partial{}^M\mathcal{B}_{0,N}, \quad {}^M\varphi_0 = {}^M\varphi_0^p \text{ on } \partial{}^M\mathcal{B}_{0,D}, \quad (1)$$

where ${}^M\mathbf{b}_0^p$ represents the body force density in the material configuration and ${}^M\mathbf{P}$ defines the macroscopic Piola stress. The traction ${}^M\mathbf{t}_0$ acts on the boundary $\partial^M\mathcal{B}_0$. The prescribed traction that acts on the Neumann portion of the boundary $\partial^M\mathcal{B}_{0,N} \subset \partial^M\mathcal{B}_0$ is denoted as ${}^M\mathbf{t}_0^p$. The displacement that is applied to the boundary $\partial^M\mathcal{B}_0$ is ${}^M\boldsymbol{\varphi}_0$. The prescribed displacement ${}^M\boldsymbol{\varphi}_0^p$ acts on the Dirichlet part of the boundary $\partial^M\mathcal{B}_{0,D} \subset \partial^M\mathcal{B}_0$. The balance of the angular momentum at the macro-scale reads

$${}^M\mathbf{P} \cdot {}^M\mathbf{F}^t = {}^M\mathbf{F} \cdot {}^M\mathbf{P}^t, \quad (2)$$

which is equivalent to the symmetry of the Cauchy stress.

2.2. Micro-problem definition

As illustrated in Fig. 2, the notations for the micro-problem mimic the macro-problem without the left superscript “M”. The kinematics of the micro-problem such as points, line elements, surface elements and volume elements from the material to spatial configuration read

$$\mathbf{x} = \boldsymbol{\varphi}(\mathbf{X}), \quad d\mathbf{x} = \mathbf{F} \cdot d\mathbf{X}, \quad ds = J \mathbf{F}^{-t} \cdot d\mathbf{S}, \quad dv = J dV. \quad (3)$$

Due to the scale separation assumption, the body forces vanish at the micro-scale. The balance of linear momentum for the micro-problem holds as

$$\text{Div} \mathbf{P} = 0 \text{ in } \mathcal{B}_0, \quad \mathbf{P} \cdot \mathbf{N} = \mathbf{t}_0 \text{ on } \partial\mathcal{B}_0, \quad \text{with} \quad \mathbf{t}_0 = \mathbf{t}_0^p \text{ on } \partial\mathcal{B}_{0,N}, \quad \boldsymbol{\varphi}_0 = \boldsymbol{\varphi}_0^p \text{ on } \partial\mathcal{B}_{0,D}. \quad (4)$$

Finally, the balance of angular momentum reads

$$\mathbf{P} \cdot \mathbf{F}^t = \mathbf{F} \cdot \mathbf{P}^t. \quad (5)$$

2.3. Micro-to-macro transition

The micro-to-macro transition is essentially a proper averaging of the quantities at the macro-scale to link them with their counterparts at the micro-scale. The advantage of the micro-to-macro transition is that no assumptions are required regarding the constitutive behavior of the material at the macro-scale. This method is capable of incorporating geometrical and physical nonlinearities without additional effort. As it is depicted in Fig. 2, the macroscopic deformation gradient is applied to the microstructure and the micro-problem is solved as a classical boundary value problem

using the finite element method. The macroscopic Piola stress is then computed via proper averaging of the micro Piola stress.

The macroscopic deformation gradient and Piola stress are related to their microscopic counterparts via averages over the volume or the boundary of the RVE as

$${}^M\mathbf{F} = \langle \mathbf{F} \rangle = \frac{1}{\mathcal{V}_0} \int_{\mathcal{B}_0} \mathbf{F} dV = \frac{1}{\mathcal{V}_0} \int_{\partial\mathcal{B}_0} \boldsymbol{\varphi} \otimes \mathbf{N} dA \quad \text{and} \quad {}^M\mathbf{P} = \langle \mathbf{P} \rangle = \frac{1}{\mathcal{V}_0} \int_{\mathcal{B}_0} \mathbf{P} dV = \frac{1}{\mathcal{V}_0} \int_{\partial\mathcal{B}_0} \mathbf{t}_0 \otimes \mathbf{X} dA. \quad (6)$$

Moreover, the Hill–Mandel condition necessitates the incremental energy equivalence between the two scales which reads

$${}^M\mathbf{P} : \delta {}^M\mathbf{F} \stackrel{!}{=} \frac{1}{\mathcal{V}_0} \int_{\mathcal{B}_0} \mathbf{P} : \delta \mathbf{F} dV, \quad (7)$$

as the volume average over the RVE. Hill's lemma, transforms Eq. (7) into a surface integral according to

$$\frac{1}{\mathcal{V}_0} \int_{\mathcal{B}_0} \mathbf{P} : \delta \mathbf{F} dV - {}^M\mathbf{P} : \delta {}^M\mathbf{F} = \int_{\partial\mathcal{B}_0} [\delta \boldsymbol{\varphi} - \delta {}^M\mathbf{F} \cdot \mathbf{X}] \cdot [\mathbf{t}_0 - {}^M\mathbf{P} \cdot \mathbf{N}] dA. \quad (8)$$

Inserting Hill's lemma (8) into the Hill–Mandel condition (7) yields

$$\int_{\partial\mathcal{B}_0} [\delta \boldsymbol{\varphi} - \delta {}^M\mathbf{F} \cdot \mathbf{X}] \cdot [\mathbf{t}_0 - {}^M\mathbf{P} \cdot \mathbf{N}] dA \stackrel{!}{=} 0, \quad (9)$$

which shall be understood as the Hill–Mandel condition in terms of a surface integral over the boundary of the RVE. Various boundary conditions can fulfill the Hill–Mandel condition a priori, see [99, 100]. Among all the boundary conditions that satisfy the Hill–Mandel condition, of practical significance are the canonical boundary conditions (i) linear displacement boundary condition (DBC), (ii) uniform traction boundary condition (TBC) and (iii) periodic displacement and anti-periodic traction (PBC) imposing

$$\text{DBC} : \boldsymbol{\varphi} = {}^M\mathbf{F} \cdot \mathbf{X}, \quad \text{TBC} : \mathbf{t}_0 = {}^M\mathbf{P} \cdot \mathbf{N} \quad \text{and} \quad \text{PBC} : [\boldsymbol{\varphi} - {}^M\mathbf{F} \cdot \mathbf{X}] \text{ and } [\mathbf{t}_0 - {}^M\mathbf{P} \cdot \mathbf{N}], \quad (10)$$

on the boundary of the RVE. For strain-driven computational homogenization here the condition ${}^M\mathbf{F} = \langle \mathbf{F} \rangle$ is a priori satisfied for both DBC and PBC. However, this is not the case for TBC and the condition ${}^M\mathbf{F} = \langle \mathbf{F} \rangle$ shall be regarded as a constraint. It is noteworthy that all the above boundary conditions satisfy the balance of angular momentum at the macro-scale. It is commonly accepted that DBC and TBC overestimate and underestimate PBC, respectively.

3. Numerical versus analytical homogenization

In this section, first the material modeling of the problem is presented. This is then followed by a brief review of the analytical methods developed to determine the overall response of composites for small strain linear elasticity. Finally, a thorough comparison of numerical and analytical results for various RVE types is provided.

3.1. Material modeling

The constituents of heterogeneous materials at the micro-scale are assumed to be hyper-elastic with known behavior. The bonding between the matrix and inclusion is considered perfect. Both matrix and inclusion behave according to the free energy density

$$\psi(\mathbf{F}) = \frac{1}{2}\mu[\mathbf{F} : \mathbf{F} - 2 - 2\log J] + \frac{1}{2}\lambda\log^2 J, \quad (11)$$

associated with a neo-Hookean response with Lamé parameters λ and μ whereby the bulk modulus associated with the plane-strain condition of interest here relates to the Lamé parameters as $\kappa = \mu + \lambda$. Using the Coleman–Noll procedure, the Piola stress is derived as

$$\mathbf{P} = \frac{\partial\psi}{\partial\mathbf{F}} = \mu[\mathbf{F} - \mathbf{F}^{-t}] + \lambda\log J \mathbf{F}^{-t}. \quad (12)$$

The corresponding fourth-order Piola tangent tensor reads

$$\mathbb{A} = \frac{\partial\mathbf{P}}{\partial\mathbf{F}} = \mu[\mathbf{I} \bar{\otimes} \mathbf{I} + \mathbf{F}^{-t} \underline{\otimes} \mathbf{F}^{-1}] + \lambda[\mathbf{F}^{-t} \otimes \mathbf{F}^{-t} - \log J \mathbf{F}^{-t} \underline{\otimes} \mathbf{F}^{-1}]. \quad (13)$$

The nonstandard tensor products $\bar{\otimes}$ and $\underline{\otimes}$ of two second-order tensors \mathbf{A} and \mathbf{B} are the forth order tensors $\mathbb{D} = \mathbf{A} \bar{\otimes} \mathbf{B}$ and $\mathbb{C} = \mathbf{A} \underline{\otimes} \mathbf{B}$, respectively, with the components $D_{ijkl} = A_{ik}B_{jl}$ and $C_{ijkl} = A_{il}B_{jk}$.

Small strain linear elasticity relates the stress $\boldsymbol{\sigma}$ to the strain $\boldsymbol{\varepsilon}$ according to the linear relation $\boldsymbol{\sigma} = \mathbb{C} : \boldsymbol{\varepsilon}$ in which the strain $\boldsymbol{\varepsilon}$ and the fourth-order constitutive tensor \mathbb{C} can be related to their counterparts at finite deformations via

$$\boldsymbol{\varepsilon} = \frac{1}{2}[\mathbf{F}^t + \mathbf{F}] - \mathbf{I} \quad \text{and} \quad \mathbb{C} = \mathbb{A}|_{\mathbf{F}=\mathbf{I}} = \mu[\mathbf{I} \bar{\otimes} \mathbf{I} + \mathbf{I} \underline{\otimes} \mathbf{I}] + \lambda[\mathbf{I} \otimes \mathbf{I}], \quad (14)$$

and the stress $\boldsymbol{\sigma}$ reads

$$\boldsymbol{\sigma} = \text{Lin } \mathbf{P} = \mathbf{P}|_{\mathbf{F}=\mathbf{I}} + \mathbb{A}|_{\mathbf{F}=\mathbf{I}} : [\mathbf{F} - \mathbf{I}] = 2\mu\boldsymbol{\varepsilon} + \lambda[\boldsymbol{\varepsilon} : \mathbf{I}]\mathbf{I}. \quad (15)$$

3.2. Analytical estimates at small strains

Analytical methods in homogenization have been established to derive a relation for the overall response of heterogeneous media. Analytical methods are based on certain simplifying assumptions so as to achieve an explicit analytical solution. In this section the most significant and extensively used analytical estimates are briefly listed. Throughout this manuscript, the matrix and inclusion properties are identified by the subscripts 1 and 2, respectively.

Voigt bounds correspond to a uniform strain field within the RVE resulting in the upper limit for the effective overall response of the material as

$$\kappa = [1 - f]\kappa_1 + f\kappa_2 \quad \text{and} \quad \mu = [1 - f]\mu_1 + f\mu_2. \quad (16)$$

where f is the inclusion volume fraction. Note that the uniform-strain assumption violates the balance of linear momentum, in general. Thus, Voigt bounds shall only be understood as an upper *unreachable* bound. Reuss bounds correspond to a uniform stress field within the RVE leading to the lower limit for the effective response of the material as

$$\kappa = \frac{\kappa_1 \kappa_2}{[1 - f]\kappa_2 + f\kappa_1} \quad \text{and} \quad \mu = \frac{\mu_1 \mu_2}{[1 - f]\mu_2 + f\mu_1}. \quad (17)$$

The uniform-stress assumption violates the compatibility of the strain field and thus, Reuss bounds shall only be understood as a lower *unreachable* bound.

Hashin and Rosen [24] proposed a predictive model based on a Composite Cylinder Assemblage (CCA) to obtain the bulk and shear moduli of transversely isotropic composites having circular inclusions in hexagonal and random arrays. The effective coefficients in this approach are frequently used to date. In this method, the upper and lower bounds on the bulk modulus coincide and read

$$\kappa_U = \kappa_L = \frac{\kappa_1 [\mu_1 + \kappa_2] + f\mu_1 [\kappa_2 - \kappa_1]}{\mu_1 + \kappa_2 + f[\kappa_1 - \kappa_2]}, \quad (18)$$

where the subscripts “U” and “L” denote the upper and the lower bounds, respectively. While the mathematical procedure of determination of bounds for the shear modulus has been addressed precisely in [24], closed form expressions

for the bounds for the shear modulus, for the first time, are given here as

$$\begin{aligned} \mu_U &= \mu_1 \left[\frac{2f[\kappa_1 + \mu_1] \left[\frac{\mu_2 - \mu_1}{\mu_2 \kappa_1 + \mu_1 \kappa_1 + 2\mu_1 \mu_2} \right]}{\frac{f[\mu_2 - \mu_1][\kappa_1 + 2\mu_1]}{\mu_2 \kappa_1 + \mu_1 \kappa_1 + 2\mu_1 \mu_2} \left[\frac{3[1-f]^2 \left[\frac{\kappa_1}{\kappa_1 + 2\mu_1} \right]^2}{f^3 \left[\frac{\mu_2 \kappa_2 [\kappa_1 + 2\mu_1] - \mu_1 \kappa_1 [\kappa_2 + 2\mu_2]}{[\kappa_1 + 2\mu_1][\kappa_2 \mu_2 + \mu_1 [\kappa_2 + 2\mu_2]]} \right] - 1} - 1 \right] + 1} + 1 \right], \\ \mu_L &= \mu_1 \left[\frac{2f[\kappa_1 + \mu_1] \left[\frac{\mu_2 - \mu_1}{\mu_2 \kappa_1 + \mu_1 \kappa_1 + 2\mu_1 \mu_2} \right]}{\frac{f[\mu_2 - \mu_1][\kappa_1 + 2\mu_1]}{\mu_2 \kappa_1 + \mu_1 \kappa_1 + 2\mu_1 \mu_2} \left[\frac{3[1-f]^2 \left[\frac{\kappa_1}{\kappa_1 + 2\mu_1} \right]^2}{f^3 \left[\frac{\mu_2 \kappa_2 [\kappa_1 + 2\mu_1] - \mu_1 \kappa_1 [\kappa_2 + 2\mu_2]}{[\kappa_1 + 2\mu_1][\kappa_2 \mu_2 + \mu_1 [\kappa_2 + 2\mu_2]]} \right] + \frac{\kappa_1}{\kappa_1 + 2\mu_1}} - 1 \right] + 1} + 1 \right]. \end{aligned} \quad (19)$$

Shortly afterwards, Hashin [101] used the variational approach in [23] to derive bounds on the overall response of fiber composites with transverse isotropy. The aim of this approach was to tighten the bounds proposed by Reuss and Voigt. The Hashin–Shtrikman bounds for the overall bulk and shear moduli read

$$\begin{aligned} \kappa_U &= \kappa_1 + \frac{f}{\frac{1}{\kappa_2 - \kappa_1} + \frac{1-f}{\kappa_1 + \mu_1}}, & \kappa_L &= \kappa_2 + \frac{[1-f]}{\frac{1}{\kappa_1 - \kappa_2} + \frac{f}{\kappa_2 + \mu_2}}, \\ \mu_U &= \mu_1 + \frac{f}{\frac{1}{\mu_2 - \mu_1} + \frac{[1-f][\kappa_1 + 2\mu_1]}{2\mu_1[\kappa_1 + \mu_1]}}, & \mu_L &= \mu_2 + \frac{[1-f]}{\frac{1}{\mu_1 - \mu_2} + \frac{f[\kappa_2 + 2\mu_2]}{2\mu_2[\kappa_2 + \mu_2]}}, \end{aligned} \quad (20)$$

for stiffness ratios less than one. The upper and the lower bound switch for stiffness ratios more than one.

The Hashin and Shtrikman variational principle [23, 101] is well-known to provide the best bounds independent of the phase geometry and are formulated only in terms of the phase properties and inclusion volume fraction. Hill [25] also derived bounds on five different effective properties of composites with transversely isotropic geometry. Walpole [27, 102] utilized piece-wise uniform polarization and rederived these bounds in a more general fashion. His method also includes anisotropic constituents and disk-shape fiber composites. All aforementioned bounds were independent of phase geometry and they were only applicable on three types of geometries; laminated, isotropic and transversely isotropic. Later, Willis [29] manipulated the Hashin–Shtrikman bounds by inserting the two-point correlation function to account for more general cases of phase geometry. If the two-point correlation function involves radial, cylindrical or disk symmetry, the above mentioned bounds could be readily recovered. See [103] for more

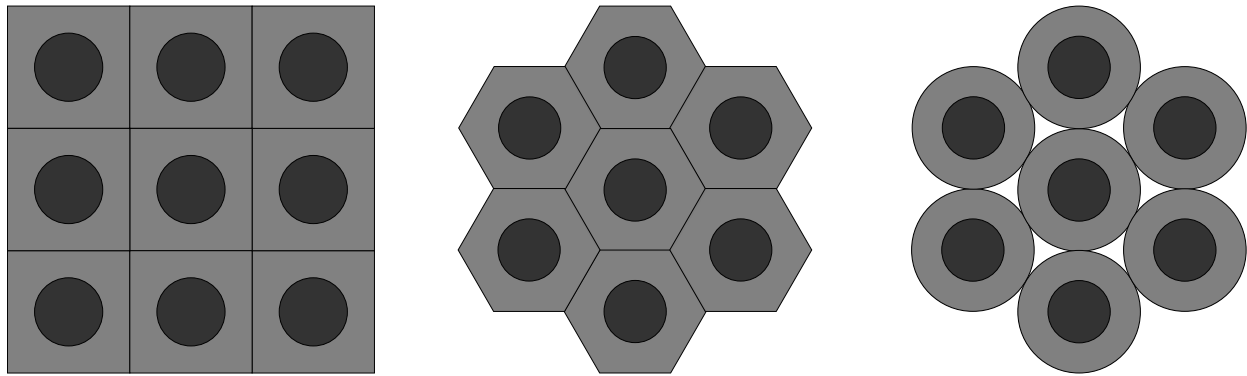


Figure 3: Packing network for each RVE. Tetragonal RVE packing (left). Hexagonal RVE packing (center) and the circular RVE packing (right). The boundaries of the tetragonal and hexagonal RVEs completely match.

details on the derivation of explicit forms for the Willis bounds.

3.3. Numerical examples

This section provides a comprehensive comparison between the analytical estimates and computational results through a series of numerical examples for tetragonal, hexagonal and circular RVEs. Figure 3 shows the packing of these RVEs. The area of each RVE is set to 1 so that the inclusion area corresponds to the volume fraction f . Obviously, the volume fraction f could not exceed a certain value for the tetragonal and hexagonal RVEs, see Fig. 4. All the examples are solved using our in-house finite element code and discretized using bi-quadratic Lagrange elements.

In order to provide a thorough and systematic comparison of the numerical and analytical results, the overall bulk modulus M_K , shear modulus M_μ and Poisson ratio M_ν of transversely isotropic composites are examined. Figure 5 clearly illustrates all the cases investigated in what follows. Five different stiffness ratios of 0.01, 0.1, 1, 10 and 100 are considered for each RVE. The stiffness ratio represents the ratio of the inclusion to matrix (incl./matr.) Lamé parameters. Stiffness ratio less than one corresponds to a more compliant inclusion within the matrix and in the limit of incl./matr. $\rightarrow 0$, the inclusion represents a void. On the contrary, the stiffness ratio more than one corresponds to a stiffer inclusion compared to matrix and in the limit of incl./matr. $\rightarrow \infty$, the inclusion acts as a rigid fiber. Throughout

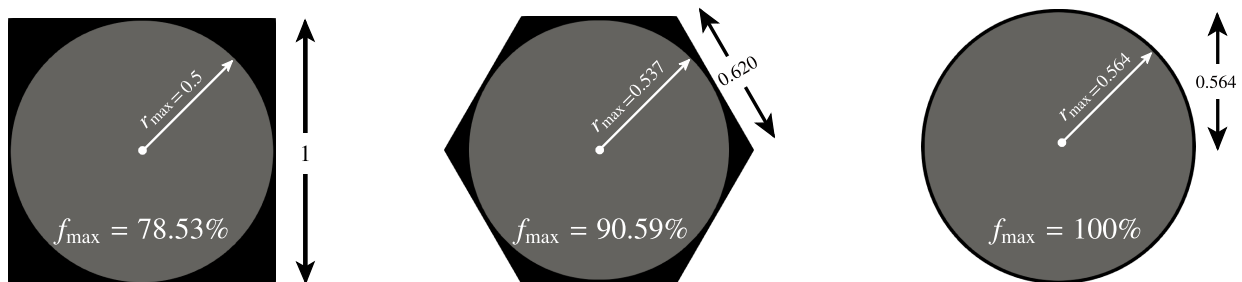


Figure 4: Maximum reachable volume fraction for each RVE. For the circular RVE, the inclusion can embed the whole RVE due its geometry.

1
2
3
4
5
6
7
8
9
10
11
12
13
14
15
16
17
18
19
20
21
22
23
24
25
26
27
28

increasing stiffness ratio
↓

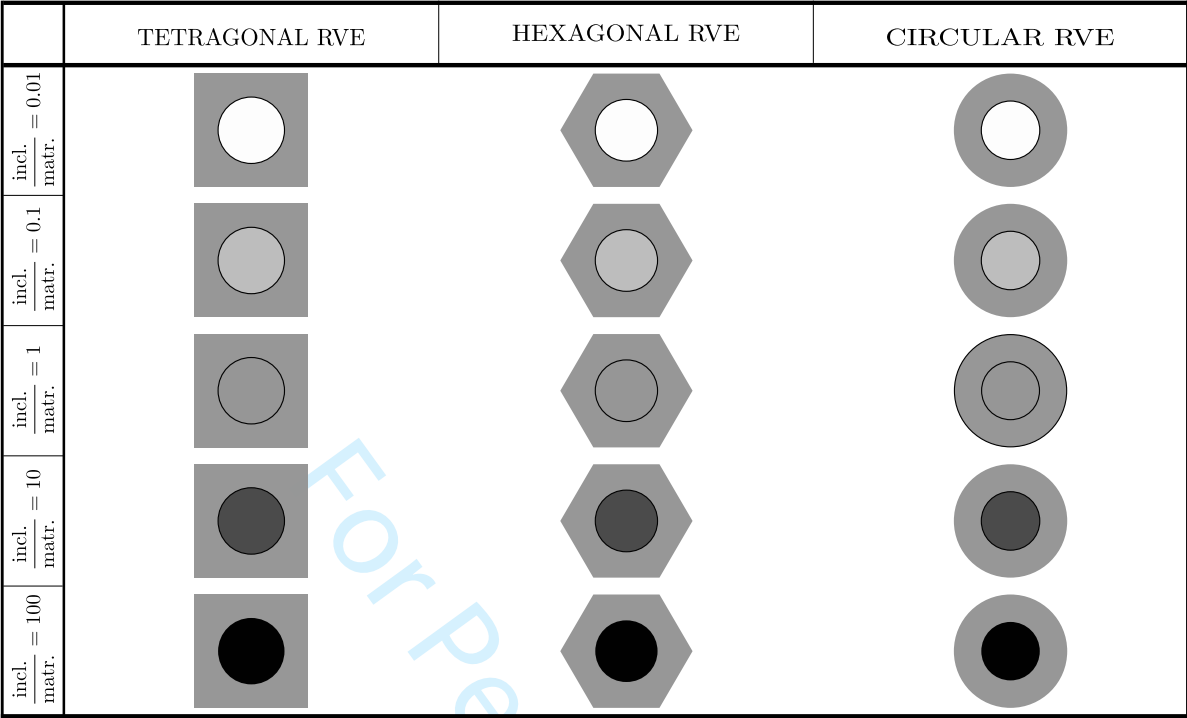


Figure 5: Different stiffness ratios for various RVE types. The columns correspond to RVE types and the rows correspond to the stiffness ratios. Matrix parameters remain the same throughout the examples while inclusion parameters vary in order to produce the required stiffness ratios. The stiffness of the inclusion is identified by a color scheme varying from light to dark.

all the examples, the matrix properties are set to $\lambda_1 = 10, \mu_1 = 10$ while the inclusion parameters vary to generate the predefined stiffness ratios.

Figure 6 shows the effective bulk modulus M_k with respect to the volume fraction f for all the cases depicted in Fig. 5. For the tetragonal and hexagonal RVEs, five individual lines represent the analytical estimates of Voigt and Reuss together with the numerical results corresponding to DBC, PBC and TBC. The RVEs in tetragonal and hexagonal packings are space-filling but cannot capture the isotropic behavior of the effective material. On the contrary, the circular RVE renders isotropic behavior and thus, comparison with the Hashin–Shtrikman and CCA approaches is justifiable. Voigt and Reuss bounds always provide reliable bounds. As expected, PBC is bounded with TBC from below and DBC from above. Moving from the tetragonal RVE towards the circular RVE, we observe that the numerical results tend to converge until they totally coincide at the circular RVE. Therefore, different boundary conditions result in same responses when the RVE is circular. Less difference between the numerical results is observed for low volume fractions. As previously mentioned, the CCA upper and lower bounds coincide while the Hashin–Shtrikman bounds do not. For $\text{incl./matr.} < 1$, a remarkable agreement is observed between the numerical results, CCA and the upper HSB (Hashin–Shtrikman bound) and for $\text{incl./matr.} > 1$, the numerical results, CCA and the lower HSB coincide. For $\text{incl./matr.} = 1$, all the results coincide since the domain is uniform.

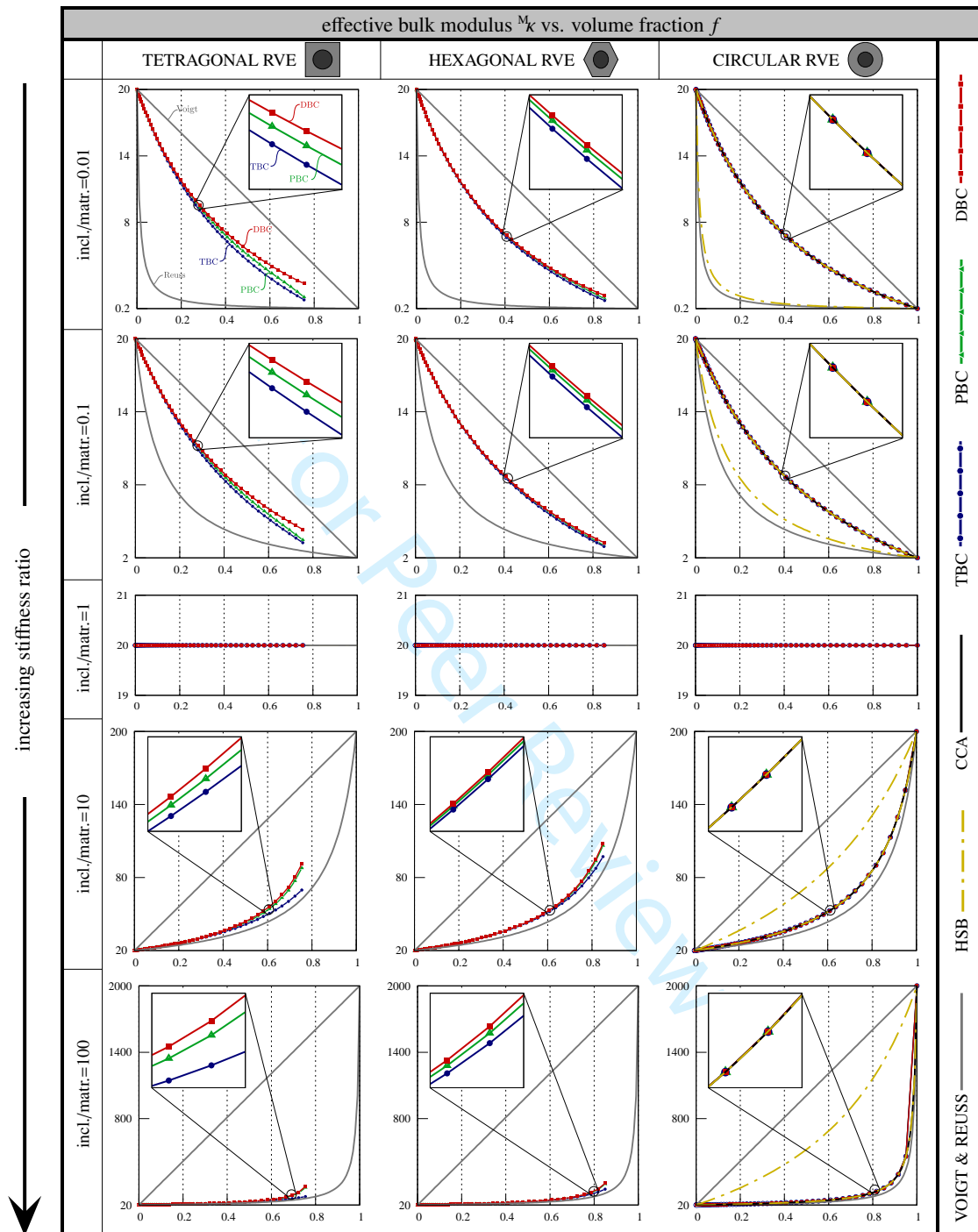


Figure 6: Effective bulk modulus versus volume fraction f . Zoom boxes are included to provide more clarity when the results are less distinguishable. The numerical results are shown by lines with points on top of them whereas the analytical results are shown using lines solely. HSB stands for Hashin–Shtrikman bounds. Composite cylinder assemblage is denoted as CCA.

Figure 7 shows the effective shear modulus M_μ versus the volume fraction for different RVEs as well as stiffness ratios. It is observed that different boundary conditions, in general, provide more distinguishable effective values

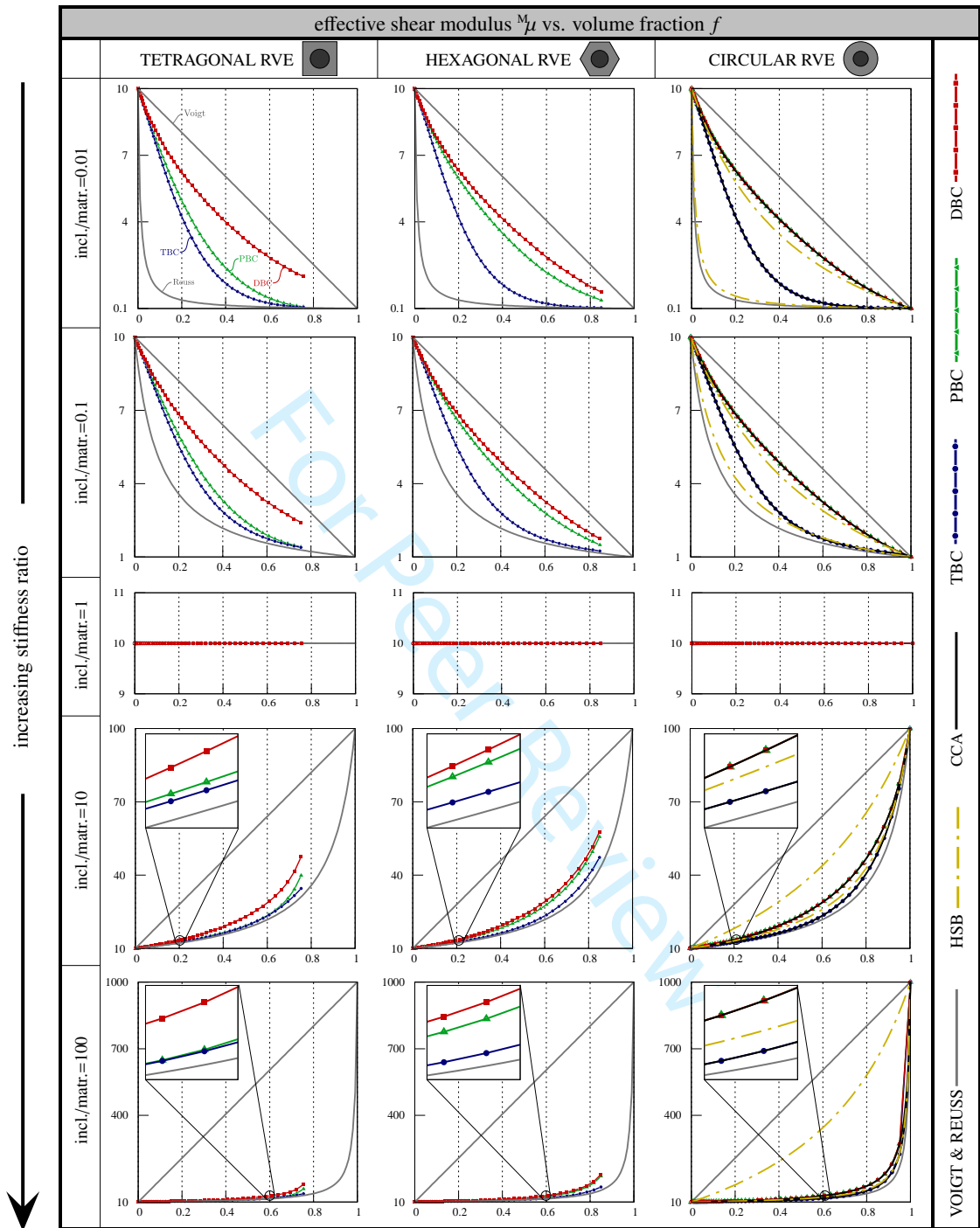


Figure 7: Effective shear modulus versus volume fraction f . Zoom boxes are included to provide more clarity when the results are less distinguishable. The numerical results are shown by lines with points on top of them whereas the analytical results are shown using lines solely. HSB stands for Hashin–Shtrikman bounds. Composite cylinder assemblage is denoted as CCA.

compared to the previous case. Nevertheless, as we move from the tetragonal RVE towards the circular RVE, PBC moves towards DBC and ultimately coincides with it. Thus, prescribing PBD and TBC to the circular RVE yield

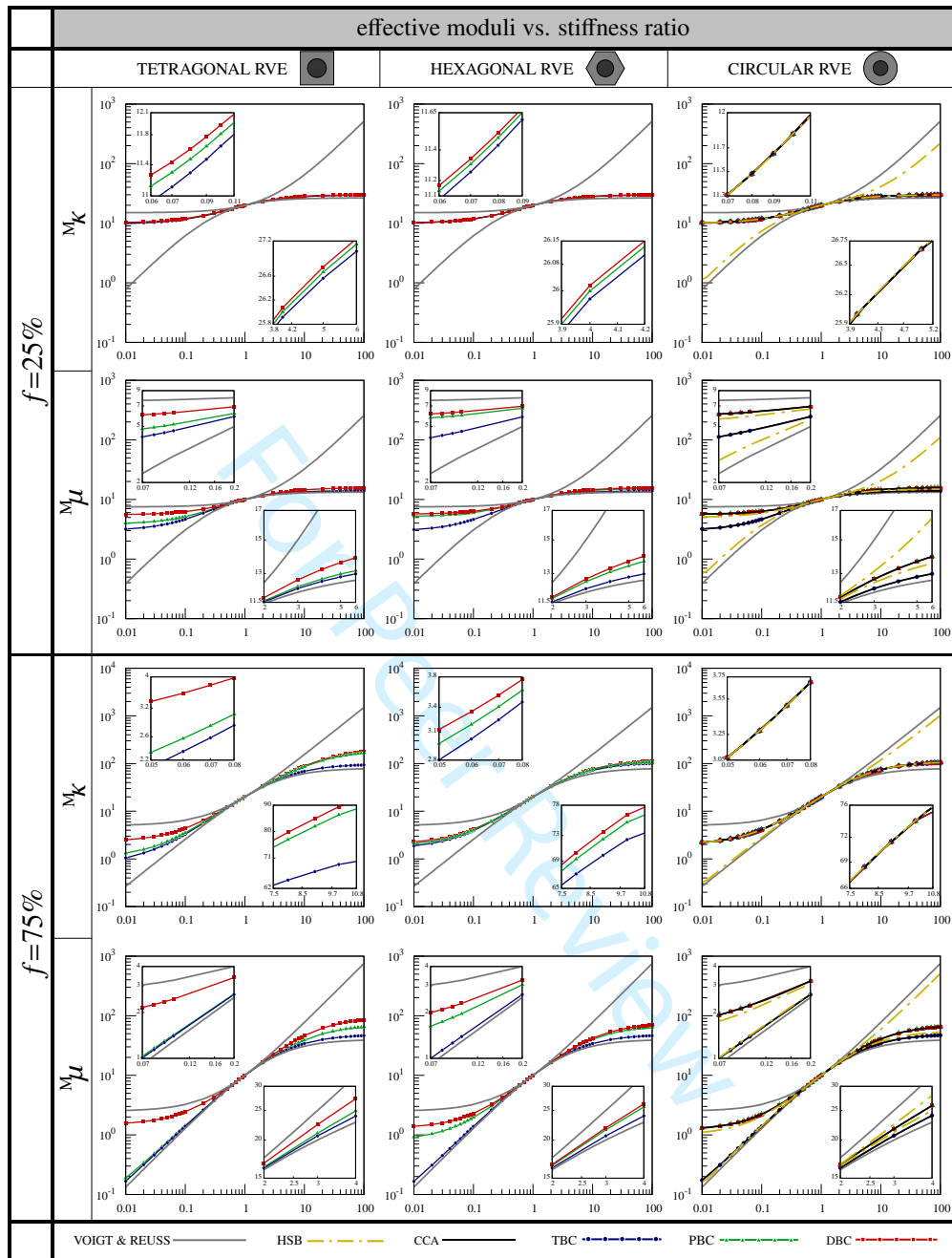


Figure 8: Overall moduli versus stiffness ratio in a logarithmic scale. Two specific volume fractions are considered that are represented in each row. A good agreement of the results is observed for the volume fraction $f = 25\%$. Increasing the volume fraction to $f = 75\%$ leads to more distinguishable results. More accordance between the results is observed for the bulk modulus M_K compared to the shear modulus M_μ . The zoom boxes provide for further clarity.

identical response. PBC renders the most sensitive numerical result to the RVE type for shear deformation. In contrast to the previous case, there is no coincidence between CCA and Hashin–Shtrikman bounds. A striking agreement is observed between CCA lower bound and TBC and between CCA upper bound and DBC/PBC. A counterintuitive

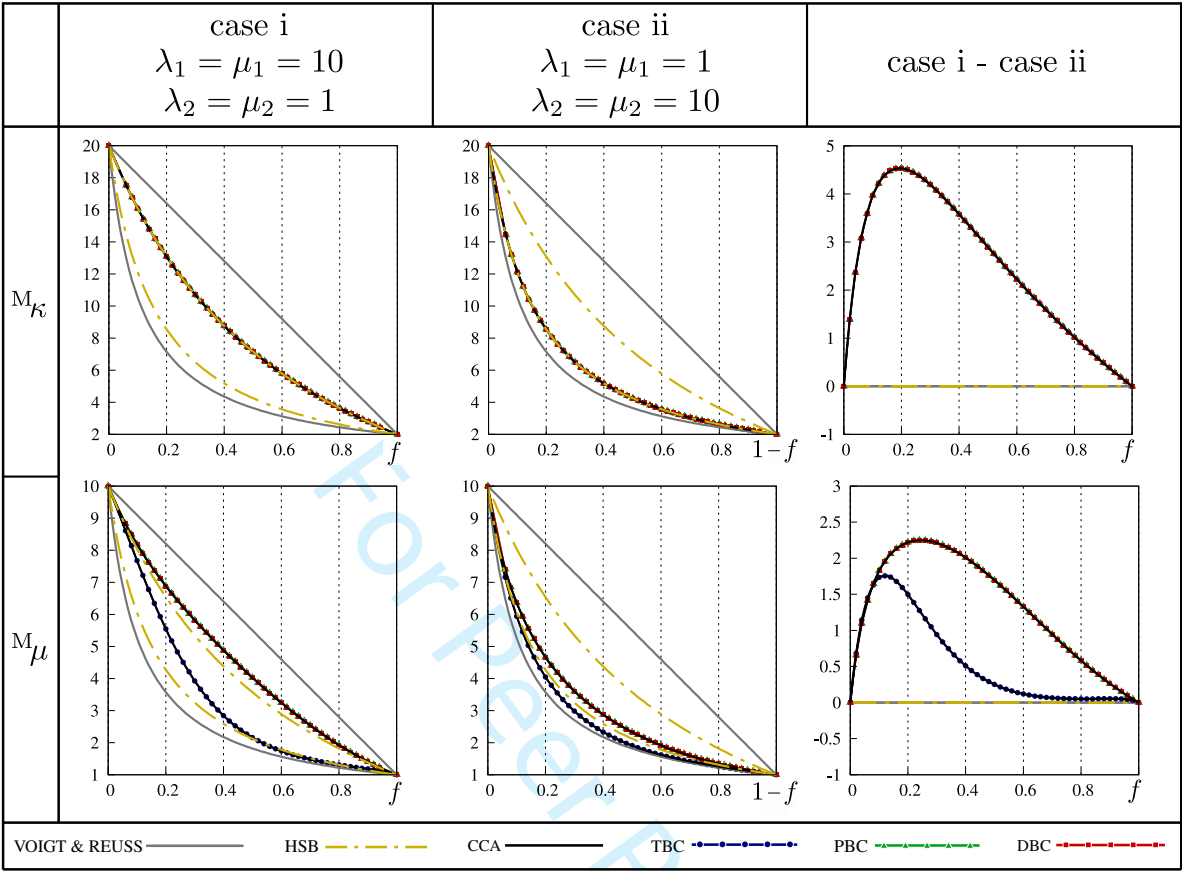


Figure 9: Illustration of the insensitivity of the Hashin–Shtrikman bounds to micro-structure’s constituents. Similarly, Voigt and Reuss bounds do not distinguish between the fiber and matrix. The numerical results depicted in this figure correspond to the circular RVE. CCA solution totally agrees with the numerical results. The first column shows $\text{incl./matr.} = 0.1$ where the inclusion and the matrix Lamé parameters are set to 1 and 10, respectively and the fiber’s volume fraction is f . The second column corresponds to $\text{incl./matr.} = 10$ where the inclusion and the matrix Lamé parameters are set to 10 and 1, respectively and the x-axis shows $1 - f$ instead of f . The third column shows the subtraction of the results in the first and the second column.

observation is that for $\text{incl./matr.} < 1$, DBC and PBC together with CCA upper bound overestimate the upper HSB and for $\text{incl./matr.} > 1$, TBC together with CCA lower bound underestimate the lower HSB. This observation shall be compared with Hashin’s remark in [104] mentioning that it has never been shown that his bounds on shear modulus are the best possible bounds. Clearly, we observe that his bounds on shear modulus do not serve as “bounds” at least not for CCA in the sense of the Voigt and Reuss bounds.

So far we have studied the effects of the variation of the volume fraction on the overall macroscopic response. Figure 8 demonstrates the variation of the effective moduli with respect to the stiffness ratio. Two different volume fractions of $f = 25\%$ and $f = 75\%$ are considered corresponding to the top row and the bottom row, respectively. As expected, all the results coincide at $\text{incl./matr.} = 1$. The gap between the results widens as stiffness ratio recedes from one. The difference between the numerical and analytical results are more distinguishable for the shear modulus M_μ compared to the bulk modulus M_K . We observe better agreement between the numerical results for the hexagonal

RVE compared to the tetragonal RVE. For the bulk modulus, the transition of the numerical results coinciding with the upper and the lower HSB for different stiffness ratios is more obvious in this figure. Another shortcoming of the Hashin–Shtrikman bounds is that similar to Voigt and Reuss bounds, they cannot distinguish between the matrix and the fiber. Figure 9 sheds light on this issue by providing a comparison of the analytical estimates and the numerical results obtained using the circular RVE. The first column correspond to a certain properties for the matrix and fiber. In the second column, the properties are switched and the results are illustrated with respect to matrix volume fraction $1 - f$. The third column shows the subtraction of the results associated with the first and second column. We observe that in contrast to the numerical results and CCA, the Voigt, Reuss and Hashin–Shtrikman bounds are incapable of distinguishing between the matrix and the fiber hence, the difference between the responses vanishes in the right column. Figure 10 illustrates the numerical results of various material properties with respect to volume fraction for the circular RVE. As observed previously, when the RVE is circular, DBC and PBC always render identical response. For the bulk modulus, DBC coincides with TBC while for the shear modulus, TBC underestimates DBC, as expected. Somewhat strikingly, for the Poisson ratio TBC overestimates DBC though. Another counterintuitive observation is that although the Poisson ratio of the fiber and matrix are identical, the overall Poisson ratio is dependent to the fiber volume fraction and is not constant.

Heterogeneous materials generally possess non-periodic or random composition to some extents. Clearly, the distribution pattern of the inclusions influences the overall material response, see [105, 106]. The next set of numerical study aims to highlight the effects of different morphologies of the micro-structures on the effective properties. To do so, we consider several RVEs with identical volume fractions of $f = 15\%$ and with random and periodic distribution of inclusions undergone the three canonical boundary conditions. The periodic micro-structure is modeled such that the inclusions of the same size are uniformly distributed throughout the RVE whereas the random micro-structures contain inclusions with different sizes and no specific order. The numerical results corresponding to the circular RVE with the same volume fraction as well as CCA and Hashin–Shtrikman bounds are also included for the sake of completeness. This study is performed for two stiffness ratios of 0.1 and 10 and the results are depicted in Figs. 11 and 12. The variation of the effective bulk modulus, shear modulus and Poisson ratio with respect to increasing the number of inclusions within the microstructure are examined. The lower Hashin–Shtrikman bound in Fig. 11 and the upper Hashin–Shtrikman bound in Fig. 12 are eliminated since they do not fit within the given range. We shall highlight that for each level of the random micro-structure, almost ten samples with different distribution patterns are investigated. That is, the effective responses shown in Figs. 11 and 12 do not correspond only to the micro-structures depicted at the bottom but reflect the average of the effective responses obtained from ten samples.

In both types of the microstructures and for both stiffness ratios, the results from DBC, PBC, and TBC tend to

1
2
3
4
5
6
7
8
9
10
11
12
13
14
15
16
17
18
19
20
21
22
23
24
25
26
27
28
29
30
31
32
33
34
35
36
37
38
39
40
41
42
43
44
45
46
47
48
49
50
51
52
53
54
55
56
57
58
59
60

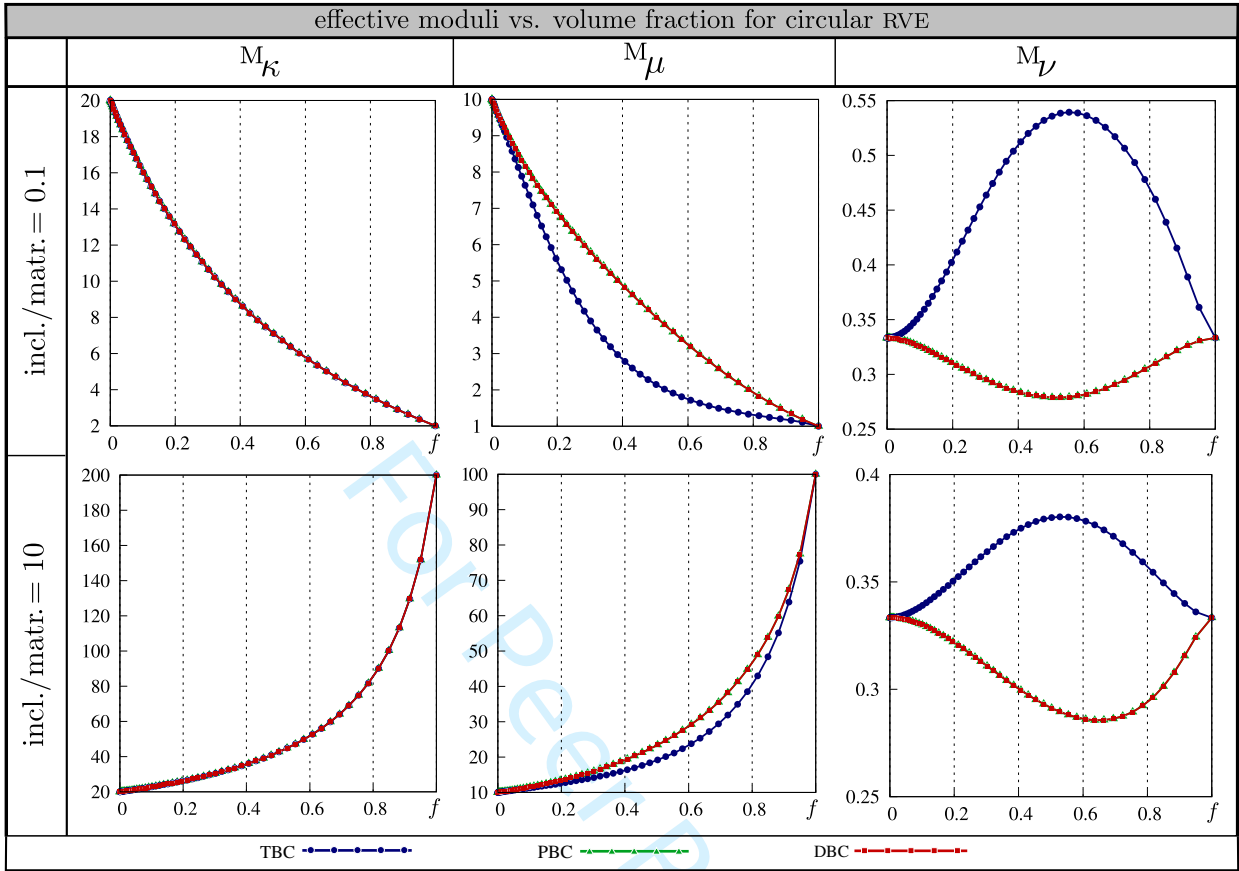


Figure 10: Illustration of different moduli versus volume fraction for two different stiffness ratios. The numerical results depicted in this figure correspond to the circular RVE. Each column corresponds to a specific material property and each row stands for specific stiffness ratio. Only numerical results are included for the Poisson ratio since analytical estimates do not provide physically meaningful results.

converge to an *effective* response as the number of inclusions increases sufficiently. This trend is smoother for the periodic micro-structure compared to the random micro-structure where some fluctuations are present. We observe that due to the periodicity of the periodic micro-structure, PBC remains constant and TBC and DBC tend to approach it from below and above, respectively. Somewhat interestingly, for the bulk modulus, the numerical results indicate that for random micro-structures and for both stiffness ratios, the circular RVE provides closer overall response to the overall response of the *true* RVE obtained by PBC. This is justified by the fact that increasing the number of inclusions within the random micro-structure resembles increasing the level of isotropy. Nonetheless, for the periodic micro-structure, increasing the number of inclusions does not alter the anisotropy of the material due to the uniform distribution of the inclusions. To be more precise, a proper case that could resemble an isotropic material suitable to be compared with analytical bounds is the random micro-structure with a large number of inclusions and randomness. Looking at the shear modulus, for the random micro-structure with large number of inclusions, the material response lies within the Hashin–Shtrikman bounds for $\text{incl./matr.} = 0.1$. However, for $\text{incl./matr.} = 10$, the lower Hashin–

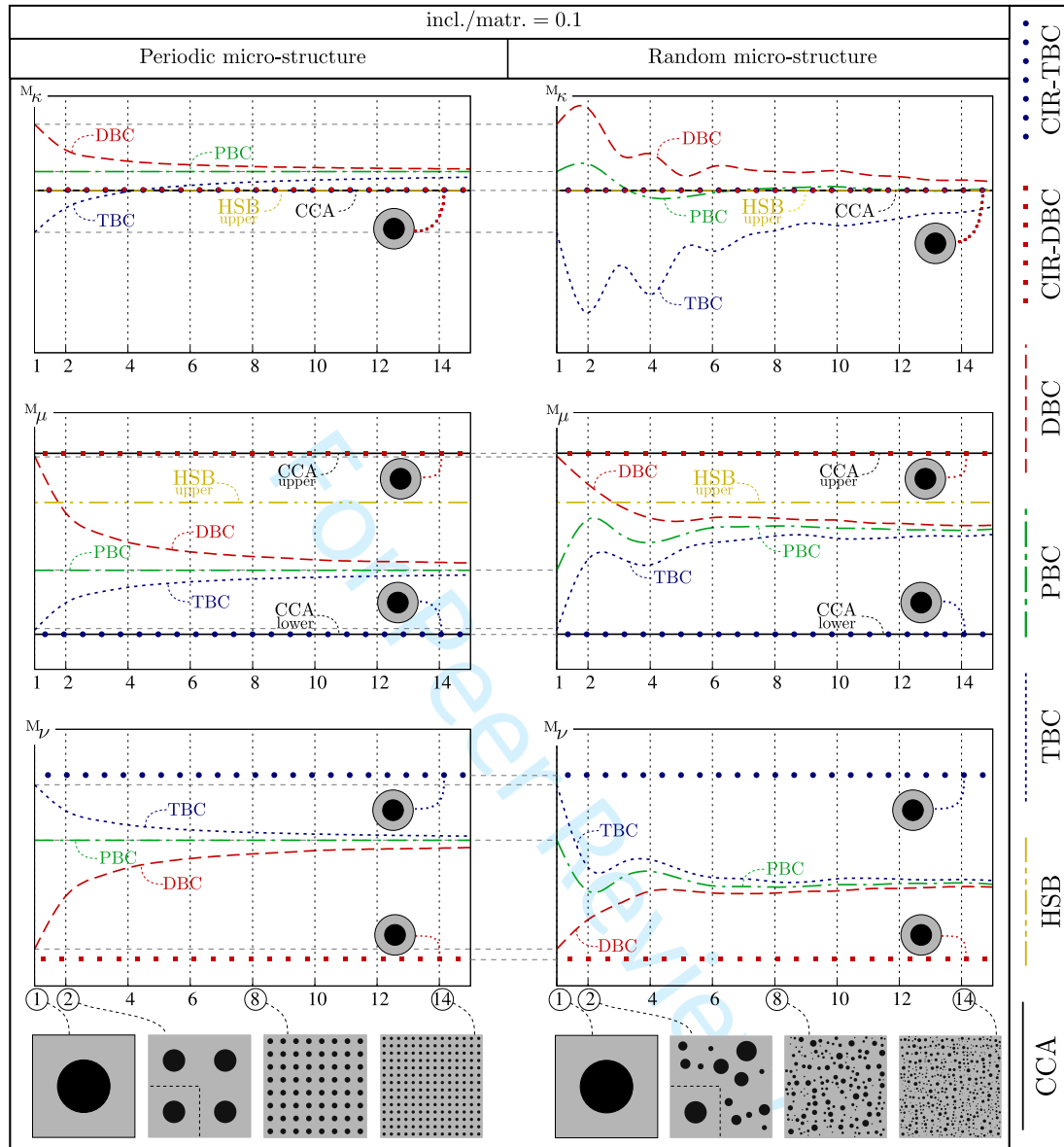


Figure 11: Illustration of the evolution of the effective properties versus the degree of periodicity and randomness for periodic and random macro-structures. Three different boundary conditions of DBC, PBC and TBC are imposed to two different micro-structures having different distribution of inclusions for stiffness ratio of 0.1. The volume fraction is set to 15%. The size of the RVE remains constant as we increase the level of periodicity or randomness. The horizontal axis shows the degree of periodicity and randomness for the periodic and random microstructure, respectively. The micro-structures for some levels are depicted at the bottom of the figure. Analytical bounds, as well as numerical results for circular RVE are included to provide further information.

Shtrikman bound is violated and fails to provide a proper bound on the shear modulus. For the Poisson ratio, unlike the shear modulus and the bulk modulus, TBC provides the stiffest response whereas DBC renders the most compliant response.

The studies carried out so far assumed that the inclusion is located at the center of the RVEs. Here we examine the effect of the inclusion eccentricity by comparing the effective response of the three RVE types due to the canonical

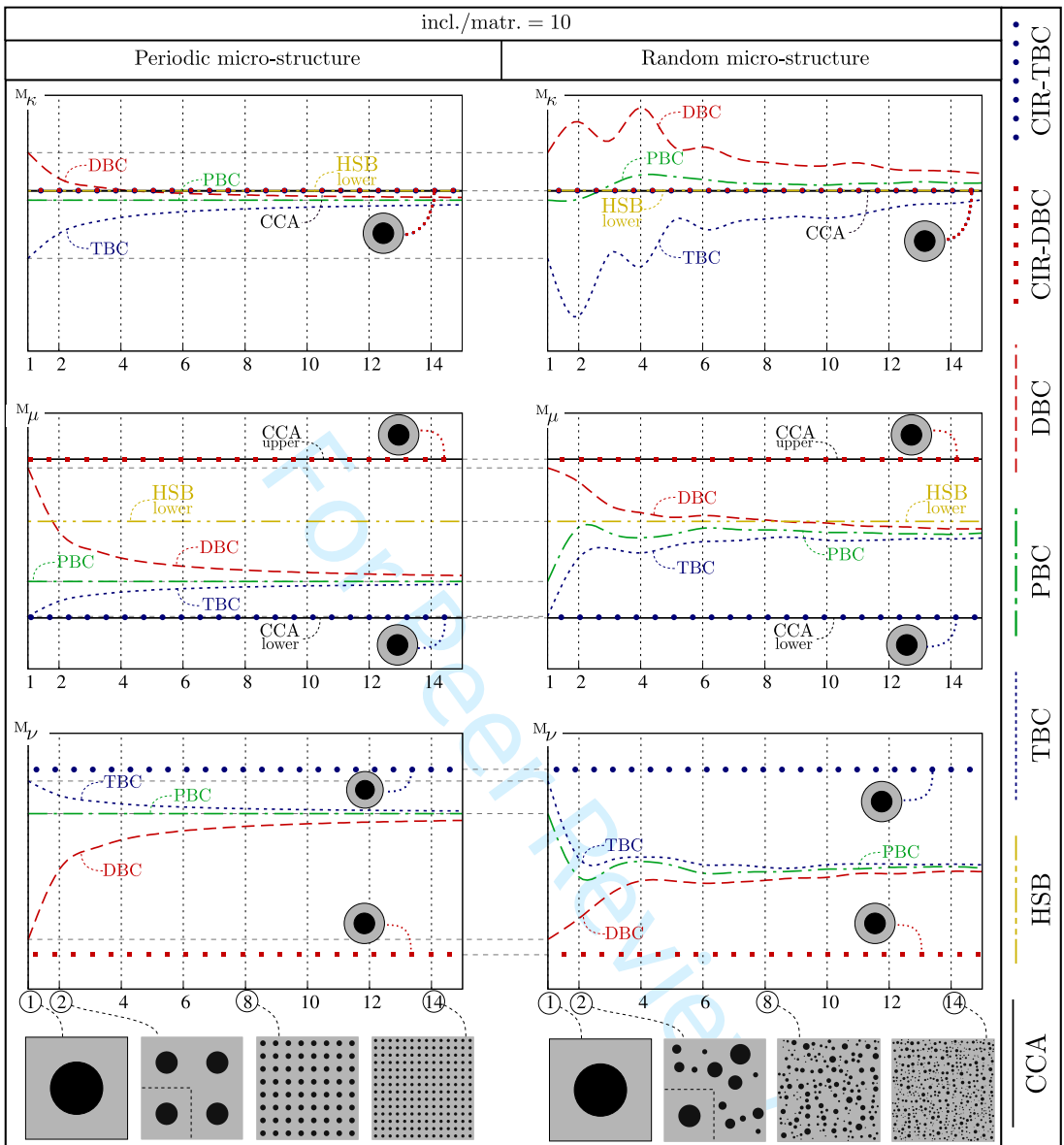


Figure 12: Illustration of the evolution of the effective properties versus the degree of periodicity and randomness for periodic and random macro-structures. Three different boundary conditions of DBC, PBC and TBC are imposed to two different micro-structures having different distribution of inclusions for stiffness ratio of 10. The volume fraction is set to 15%. The size of the RVE remains constant as we increase the level of periodicity or randomness. The horizontal axis shows the degree of periodicity and randomness for the periodic and random microstructure, respectively. The micro-structures for some levels are depicted at the bottom of the figure. Analytical bounds, as well as numerical results for circular RVE are included to provide further information.

boundary conditions for different volume fractions as well as different stiffness ratios. Figures 13 and 14 provide the deformed shapes of the RVEs as well as the overall response of the material due to volumetric expansion and simple shear, respectively, for $\text{incl./matr.} = 0.1$. The numerical examples correspond to small-strain linear elasticity but deformations are magnified for the sake of illustration. Additionally, the distribution of $[\sigma_{11} + \sigma_{22}]/2$ for the expansion case and σ_{12} for the shear case is displayed throughout each RVE. Each block includes four cases corresponding to

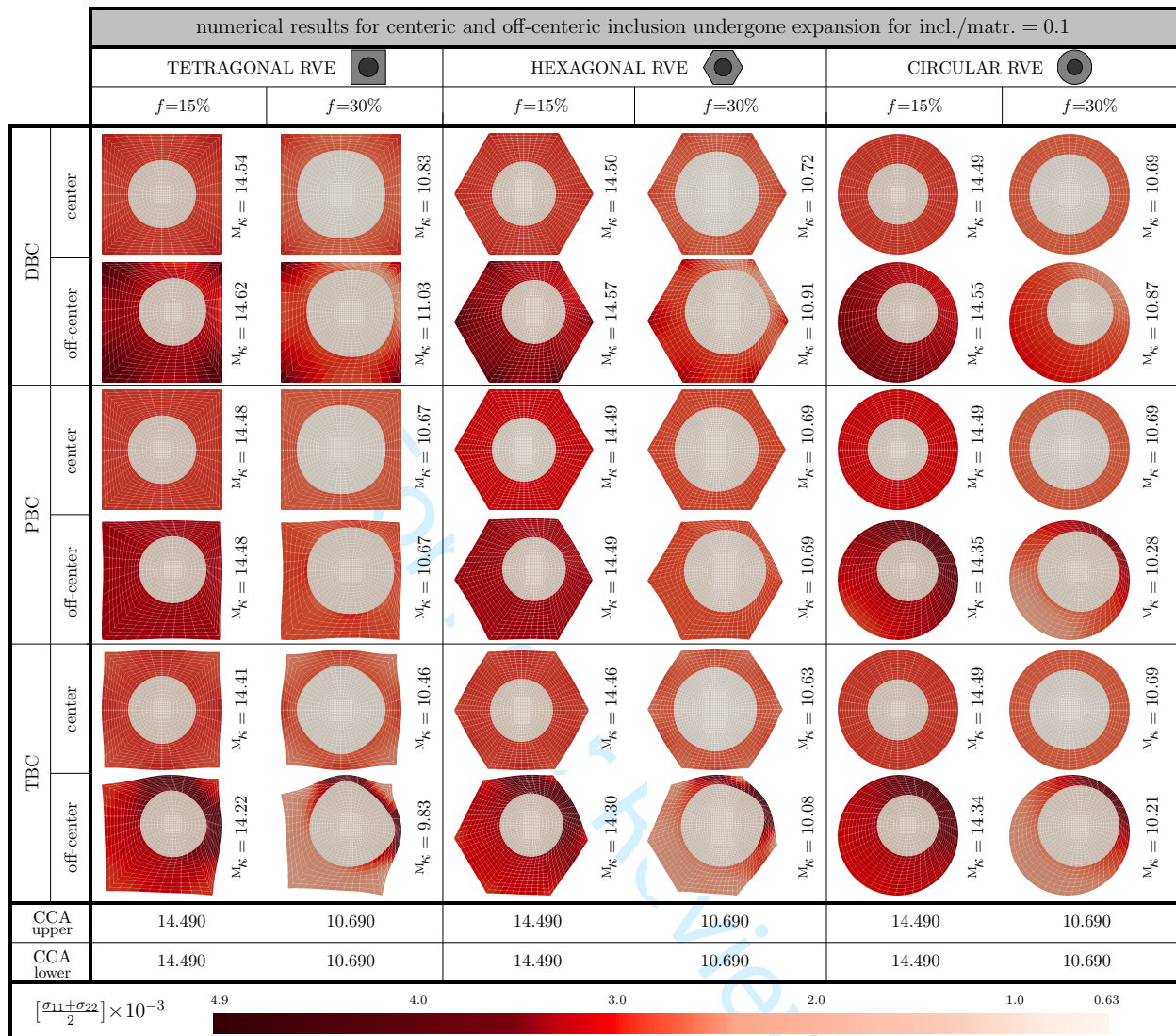


Figure 13: Stress distribution within the RVE undergone simple shear for both centeric and off-centeric inclusions when the inclusion is more compliant to the matrix (incl./matr. = 0.1). The distribution of the stress component $[\sigma_{11} + \sigma_{22}]/2$ is shown throughout the RVE. Two volume fractions $f = 15\%$ and $f = 30\%$ are considered. CCA bounds on the overall bulk modulus are given for comparison. PBC always lies within TBC and DBC. Three main rows correspond to three boundary conditions and three main columns correspond to three different RVEs. For each boundary condition the centeric and off-centeric inclusion as well as two different volume fractions are examined.

the centeric and off-centeric inclusion for different volume fractions. CCA lower and upper bounds are also included to serve as a comparison.

The difference between the results is more distinguishable for $f = 30\%$ than $f = 15\%$. As expected, the effective bulk modulus for $f = 30\%$ is, in all cases, less than its counterpart for $f = 15\%$. For all the RVEs, when DBC is prescribed, the off-centeric inclusion leads to a stiffer response compared to the centeric one. In contrast, if TBC is imposed, the effective modulus corresponding to the RVE with off-centeric inclusion underestimates the one with

1
2
3
4
5
6
7
8
9
10
11
12
13
14
15
16
17
18
19
20
21
22
23
24
25
26
27
28
29
30
31
32
33
34
35
36
37
38
39
40
41
42
43
44
45
46
47
48
49
50
51
52
53
54
55
56
57
58
59
60

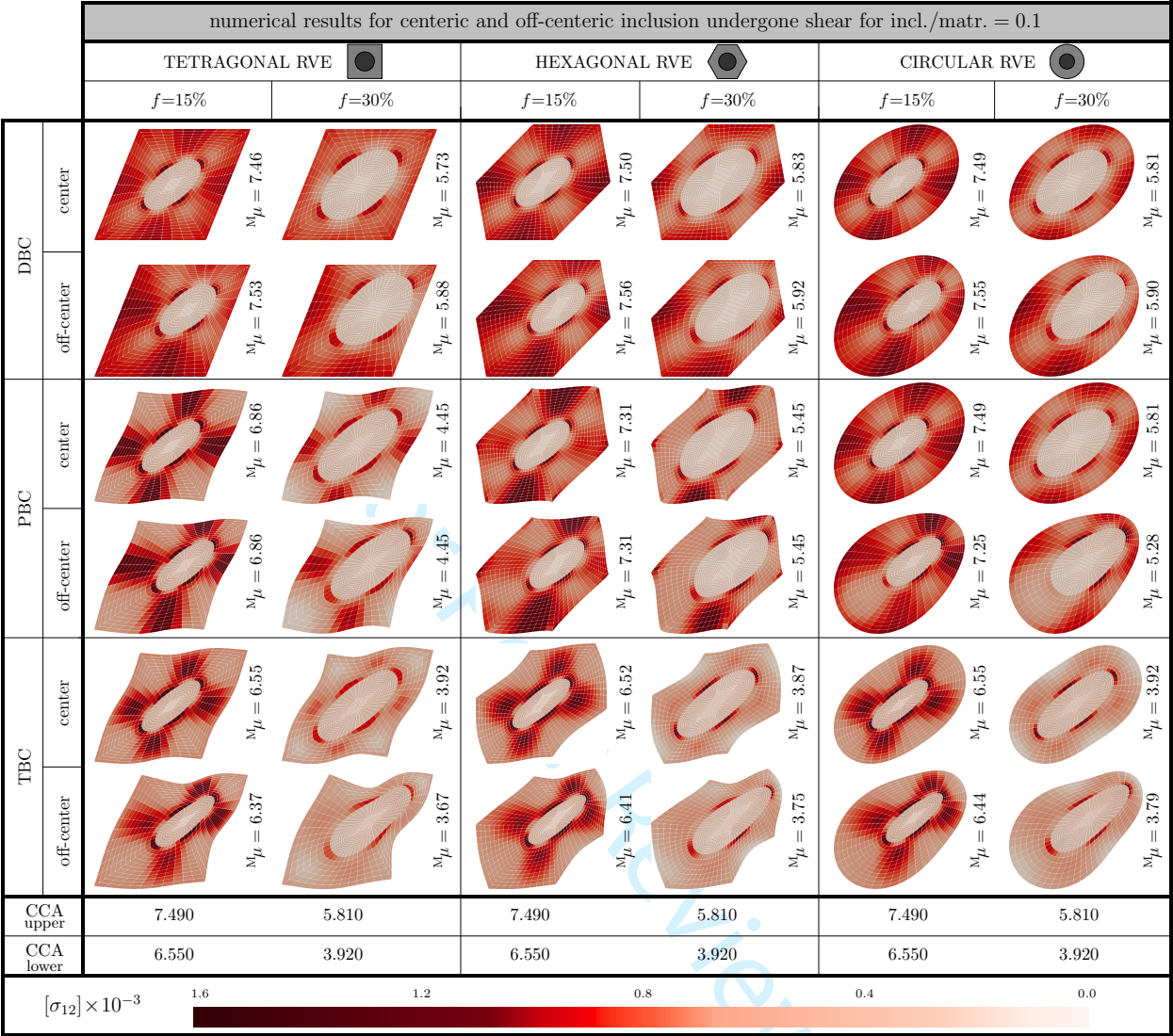


Figure 14: Stress distribution within the RVE undergone simple shear for both centric and off-centric inclusions when the inclusion is more compliant to the matrix (incl./matr. = 0.1). The distribution of the stress component σ_{12} is shown throughout the RVE. Two volume fractions $f = 15\%$ and $f = 30\%$ are considered. CCA bounds on the overall shear modulus are given for comparison. PBC always lies within TBC and DBC. Three main rows correspond to three boundary conditions and three main columns correspond to three different RVEs. For each boundary condition the centric and off-centric inclusion as well as two different volume fractions are examined.

centric inclusion. When the inclusion is at the center of the circular RVE, all the results are identical for a given volume fraction. Somewhat interestingly, when PBC is employed, the overall response becomes independent of the inclusion position for the tetragonal and hexagonal RVEs. However, for the circular RVE, the material renders stiffer response for the centric inclusion than off-centric one. Figures 15 and 16 are the counterparts for Figs. 13 and 14, respectively, corresponding to incl./matr. = 10. The effective moduli at $f = 30\%$ for all the cases here, are larger than their counterparts at $f = 15\%$. The remainder of the observations in Figs. 15 and 16 are similar to those made from

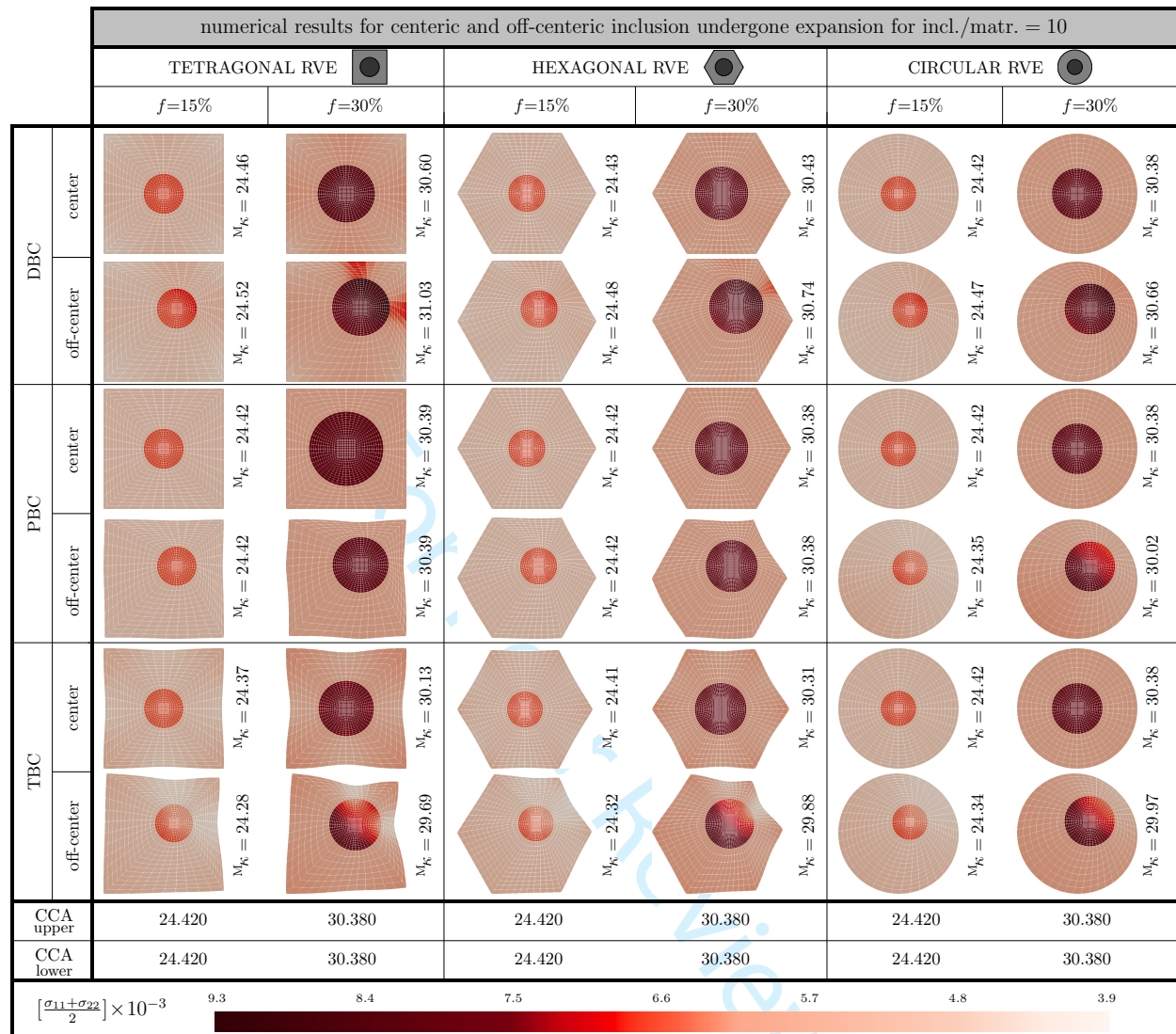


Figure 15: Stress distribution within the RVE undergone volumetric expansion for both centric and off-centric inclusions when the inclusion is stiffer to the matrix (incl./matr. = 10). The distribution of the stress component $[\sigma_{11} + \sigma_{22}]/2$ is shown throughout the RVE. Two volume fractions $f = 15\%$ and $f = 30\%$ are considered. CCA bounds on the overall bulk modulus are given for comparison. PBC always lies within TBC and DBC. Three main rows correspond to three boundary conditions and three main columns correspond to three different RVEs. For each boundary condition the centric and off-centric inclusion as well as two different volume fractions are examined.

Figs. 13 and 14 hence, their discussion is omitted for the sake brevity.

4. Extension to finite deformations

All the previous examples were only valid at small strains. The main objective of this section is to extend the numerical studies presented in the last section to finite deformations setting. In doing so, two load cases of volumetric expansion and simple shear are prescribed and the effective material response is computed via proper averaging. The examples

1
2
3
4
5
6
7
8
9
10
11
12
13
14
15
16
17
18
19
20
21
22
23
24
25
26
27
28
29
30
31
32
33
34
35
36
37
38
39
40
41
42
43
44
45
46
47
48
49
50
51
52
53
54
55
56
57
58
59
60

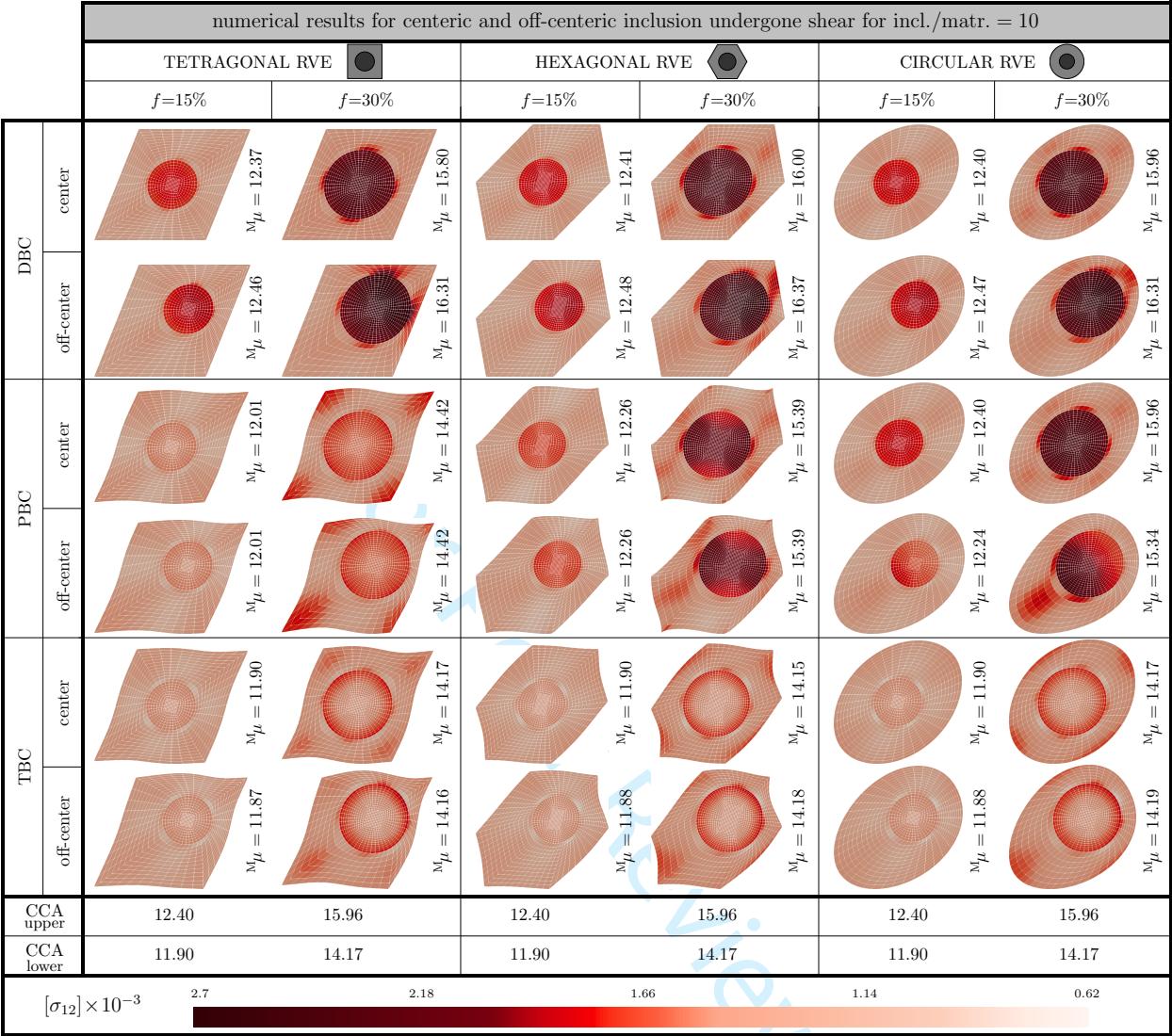


Figure 16: Stress distribution within the RVE undergone simple shear for both centric and off-centric inclusions when the inclusion is stiffer to the matrix (incl./matr. = 10). The distribution of the stress component σ_{12} is shown throughout the RVE. Two volume fractions $f = 15\%$ and $f = 30\%$ are considered. CCA bounds on the overall shear modulus are given for comparison. PBC always lies within TBC and DBC. Three main rows correspond to three boundary conditions and three main columns correspond to three different RVEs. For each boundary condition the centric and off-centric inclusion as well as two different volume fractions are examined.

carefully analyze the overall material response for various boundary conditions and stiffness ratios. Unlike in small-strain linear elasticity, for finite deformations it is not possible to define an effective material parameter such as bulk modulus or shear modulus. Therefore, in what follows the apparent macroscopic quantity of interest is the stress itself. For instance, for volumetric expansion, the xx -component of the Piola stress and for simple shear, the xy -component of the Piola stress are the macroscopic properties of interest.

Figure 17 shows the variation of the macro Piola stress with respect to the volume fraction for various RVEs

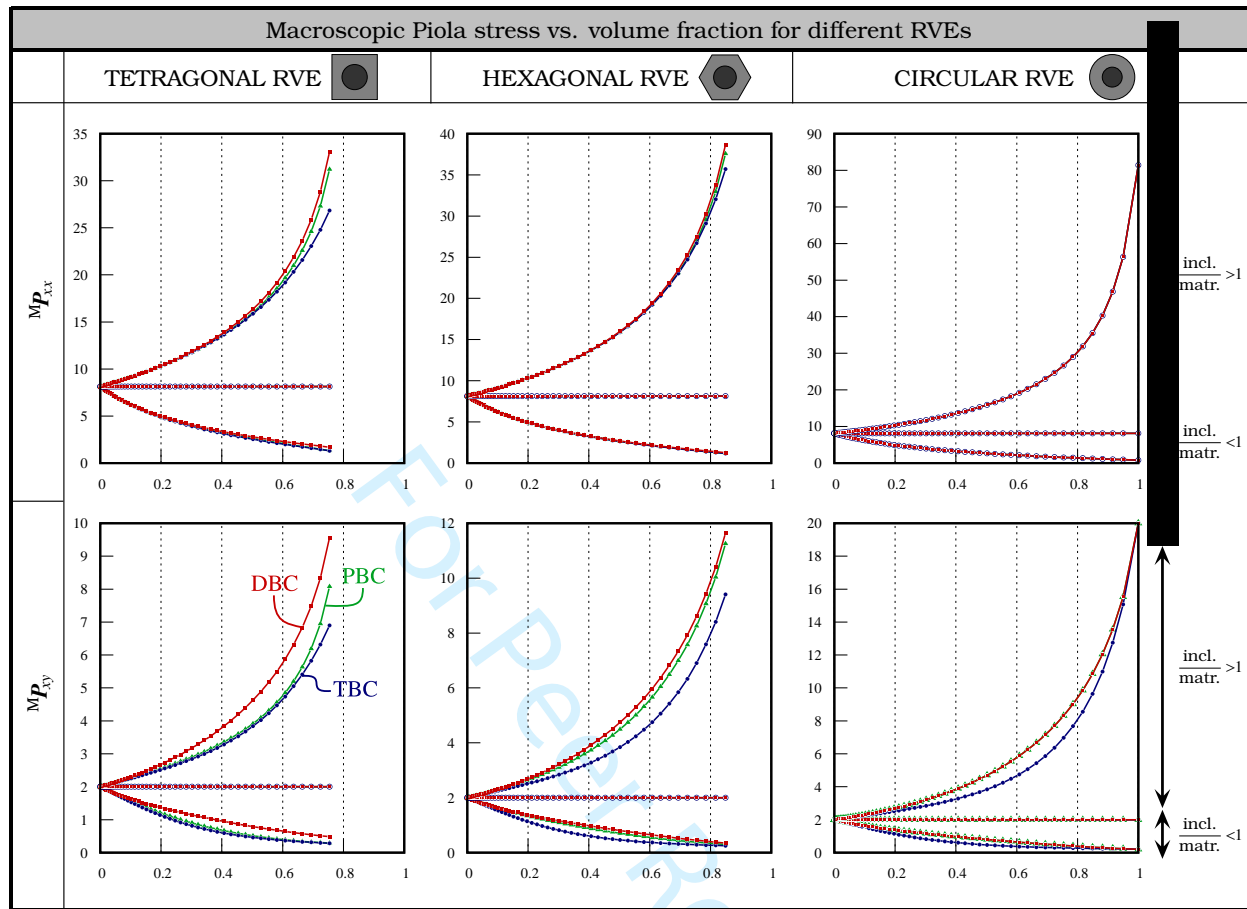


Figure 17: Macro Piola stress with respect to the volume fraction f for various types of RVE. The first row is associated with the volumetric expansion and thus the macroscopic stress component of interest is M_{xx} . The bottom row corresponds to the simple shear deformation and thus the macroscopic stress component of interest is M_{xy} . Each column corresponds to specific RVE. At each plot, different boundary conditions for a specific RVE are examined.

obtained from different boundary conditions. The first row represents the volumetric expansion case while the second row corresponds to the simple shear, both at 20% deformation. First consider the first row corresponding to the expansion case. As expected, PBC is bounded with TBC from below and DBC from above. For the tetragonal RVE, the results from different boundary conditions mostly deviate from each other as the volume fraction increases. However, as we move towards the circular RVE the results get closer to each other and coincide eventually. Next consider the second row corresponding to the shear case. For this case, more difference between the numerical results is observed in comparison to the expansion case. The results from PBC are closer to TBC for the tetragonal RVE. For the hexagonal RVE PBC renders closer response to DBC and for the circular RVE they result in identical response. These observation elucidates the sensitivity of PBC to the RVE type.

Figure 18 depicts the variation of the macro Piola stress with respect to the volume fraction for different boundary conditions. The top row correspond to the expansion case and the bottom row correspond to the simple shear case.

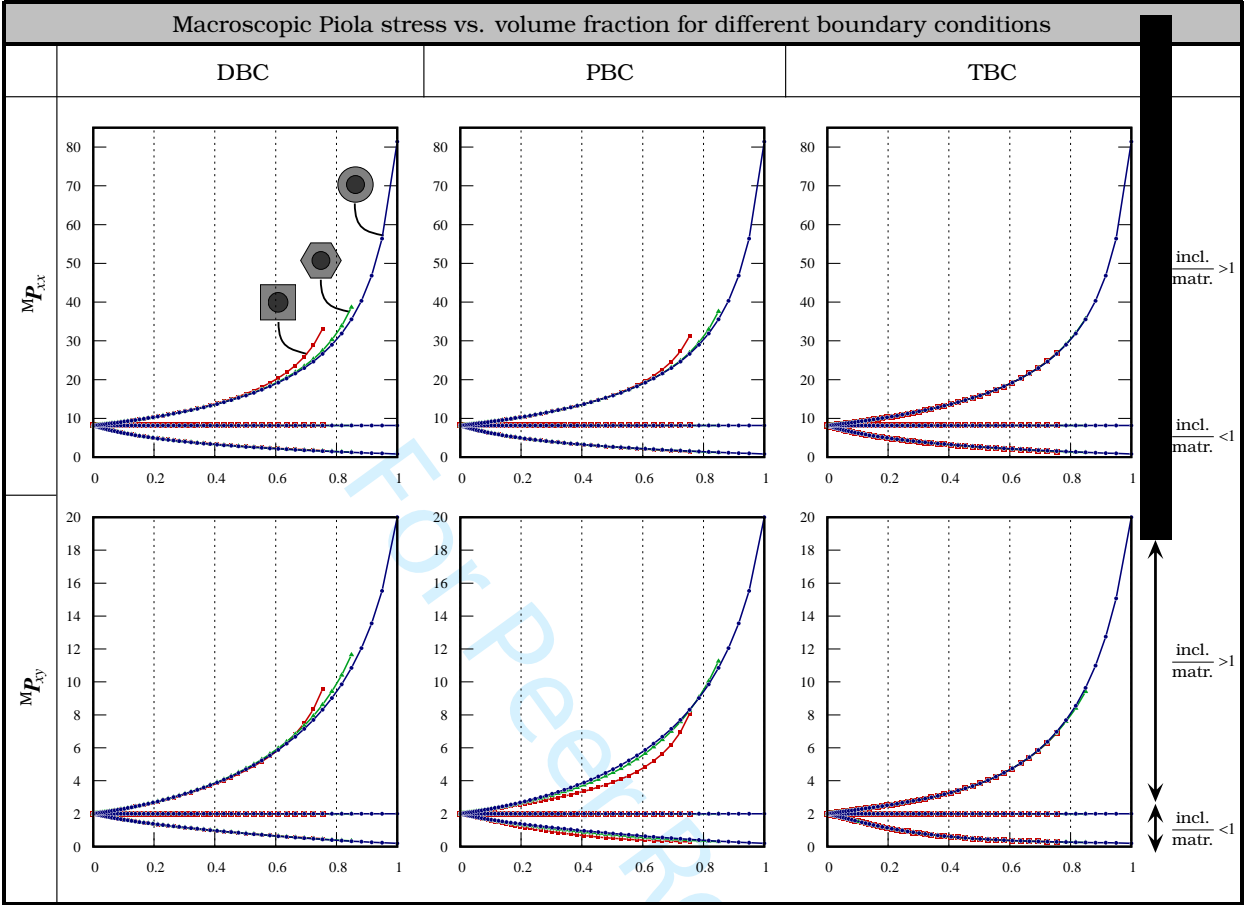


Figure 18: Macro Piola stress with respect to the volume fraction f for boundary conditions. The first row is associated with the volumetric expansion and thus the macroscopic stress component of interest is $M_{P_{xx}}$. The bottom row corresponds to the simple shear deformation and thus the macroscopic stress component of interest is $M_{P_{xy}}$. Each column corresponds to specific boundary condition. At each plot, different RVE types for a specific boundary condition are examined.

As mentioned before, the circular RVE is able to reach to higher volume fractions compared to the other RVEs. For DBC, it is observed that the stress corresponding to the hexagonal RVE is bounded between the tetragonal RVE from above and the circular RVE from below. For PBC, the same observation is made when expansion is applied. However, when shear is applied, tetragonal RVE results in the lowest Piola stress while the hexagonal and circular RVE render different relative behavior depending on the volume fraction. For TBC, there is a remarkable coincidence between all the numerical results for both expansion and shear case. This means that TBC is indifferent to the type of the RVE. This observation highlights the importance of frequently disregarded TBC in computational homogenization.

5. Conclusion and outlook

In summary, we have presented a systematic comparison on the overall behavior of heterogeneous materials via both analytical and computational homogenization. It is clearly demonstrated that in contrast to the Voigt and Reuss bounds, for some cases the Hashin-Shtrikman bounds do not provide reliable bounds on the shear modulus. Three different material properties i.e. bulk modulus, shear modulus and Poisson ratio were comprehensively studied for various RVEs, boundary conditions and micro-structures. Our findings show that among all the simplified RVE types, the circular RVE serves as the most suitable RVE to predict overall *isotropic* material behavior due to its intrinsic feature to capture isotropy. The influence of the inclusion eccentricity on the effective modulus of the material is examined. For both the tetragonal and hexagonal packings, the numerical results based on PBC are indifferent with respect to the inclusion position in the RVE. The numerical results are then extended to the finite deformation setting and it is observed that TBC shows less sensitivity with respect to the RVE type. This conclusion is particularly interesting since TBC is often disregarded in computational homogenization. Our next immediate extension of this contribution deals with a complimentary study accounting for size effects. Further extensions of this work include three-dimensional analysis as well as including more complex analytical estimates.

6. Acknowledgments

The support of this work by the Cluster of Excellence “Engineering of Advanced Materials” at the University of Erlangen-Nuremberg, funded by the DFG within the framework of its “Excellence Initiative”, is greatly appreciated. Also, Ali Javili would like to thank Christian Linder for inspiring discussions regarding the circular RVE.

References

- [1] J. Broughton, F. Abraham, N. Bernstein, E. Kaxiras, Concurrent coupling of length scales: Methodology and application, *Phys. Rev. B* 60 (1999) 2391–2403.
- [2] J. T. Oden, K. Vemaganti, N. Moes, Hierarchical modeling of heterogeneous solids, *Comput. Methods Appl. Mech. Eng.* 172 (1999) 3–25.
- [3] S. Ghosh, J. Bai, P. Raghavan, Concurrent multi-level model for damage evolution in microstructurally debonding composites, *Mech. Mater.* 39 (2007) 241–266.
- [4] A. R. Khoei, F. Jahanbakhshi, A. Aramoon, A concurrent multi-scale technique in modeling heterogeneous FCC nano-crystalline structures, *Mech. Mater.* 83 (2015) 40–65.
- [5] P. M. Suquet, *Elements of Homogenization Theory for Inelastic Solid Mechanics*, *Homogenization Techniques for Composite Media* (1987) 194–278.
- [6] H. Moulinec, P. Suquet, A numerical method for computing the overall response of nonlinear composites with complex microstructure, *Computer Methods in Applied Mechanics and Engineering* 157 (1998) 69–94.
- [7] P. Ponte Castañeda, P. Suquet, *Nonlinear Composites*, *Adv. Appl. Mech.* 34 (1997) 171–302.

- [8] O. van der Sluis, P. Vosbeek, P. Schreurs, H. Jer, Homogenization of heterogeneous polymers, *Int. J. Solids Struct.* 36 (1999) 3193–3214.
- [9] T. I. Zohdi, P. Wriggers, Computational micro-macro material testing, *Arch. Comput. Methods Eng.* 8 (2001) 131–228.
- [10] V. Kouznetsova, M. G. D. Geers, W. A. M. Brekelmans, Multi-scale constitutive modelling of heterogeneous materials with a gradient-enhanced computational homogenization scheme, *Int. J. Numer. Methods Eng.* 54 (2002) 1235–1260.
- [11] O. Lloberas-Valls, D. J. Rixen, A. Simone, L. J. Sluys, On micro-to-macro connections in domain decomposition multiscale methods, *Comput. Methods Appl. Mech. Eng.* 225 (2012) 177–196.
- [12] X. Li, Q. Liu, J. Zhang, A micro-macro homogenization approach for discrete particle assembly - Cosserat continuum modeling of granular materials, *Int. J. Solids Struct.* 47 (2010) 291–303.
- [13] N. Willoughby, W. J. Parnell, A. L. Hazel, I. D. Abrahams, Homogenization methods to approximate the effective response of random fibre-reinforced Composites, *Int. J. Solids Struct.* 49 (2012) 1421–1433.
- [14] W. G. Jiang, R. Z. Zhong, Q. H. Qin, Y. G. Tong, Homogenized finite element analysis on effective elastoplastic mechanical behaviors of composite with imperfect interfaces, *Int. J. Mol. Sci.* 15 (2014) 23389–23407.
- [15] A. Raina, C. Linder, A homogenization approach for nonwoven materials based on fiber undulations and reorientation, *J. Mech. Phys. Solids* 65 (2014) 12–34.
- [16] R. Hill, Elastic properties of reinforced solids: Some theoretical principles, *J. Mech. Phys. Solids* 11 (1963) 357–372.
- [17] R. Hill, On Constitutive Macro-Variables for Heterogeneous Solids at Finite Strain, *Proceedings of the Royal Society A: Mathematical, Physical and Engineering Sciences* 326 (1972) 131–147.
- [18] R. Ogden, On the overall moduli of non-linear elastic composite materials, *Journal of the Mechanics and Physics of Solids* 22 (1974) 541–553.
- [19] J. Mandel, Contribution théorique à l'étude de l'écrouissage et des lois de l'écoulement plastique, in: *Appl. Mech.*, Springer Berlin Heidelberg, 502–509, 1966.
- [20] W. Voigt, Ueber die Beziehung zwischen den beiden Elasticitätsconstanten isotroper Körper, *Ann. Phys.* 274 (1889) 573–587.
- [21] A. Reuss, Berechnung der Fließgrenze von Mischkristallen auf Grund der Plastizitätsbedingung für Einkristalle, *ZAMM* 9 (1929) 49–58.
- [22] J. D. Eshelby, The Determination of the Elastic Field of an Ellipsoidal Inclusion, and Related Problems, *Proc. R. Soc. A Math. Phys. Eng. Sci.* 241 (1957) 376–396.
- [23] Z. Hashin, S. Shtrikman, A variational approach to the theory of the elastic behaviour of multiphase materials, *J. Mech. Phys. Solids* 11 (1963) 127–140.
- [24] Z. Hashin, B. Rosen, The elastic moduli of fiber-reinforced materials, *J. Appl. Mech.* 31 (1964) 223–232.
- [25] R. Hill, Theory of mechanical properties of fibre-strengthened materials: I. Elastic behaviour, *J. Mech. Phys. Solids* 12 (1964) 199–212.
- [26] R. Hill, A self-consistent mechanics of composite materials, *J. Mech. Phys. Solids* 13 (1965) 213–222.
- [27] L. J. Walpole, On the overall elastic moduli of composite materials, *J. Mech. Phys. Solids* 17 (1969) 235–251.
- [28] T. Mori, K. Tanaka, Average stress in matrix and average elastic energy of materials with misfitting inclusions, *Acta Metall.* 21 (1973) 571–574.
- [29] J. R. Willis, Bounds and self-consistent estimates for the overall properties of anisotropic composites, *J. Mech. Phys. Solids* 25 (1977) 185–202.
- [30] S. Nemat-Nasser, T. Iwakuma, Elastic-plastic composites at finite strains, *Int. J. Solids Struct.* 21 (1985) 55–65.
- [31] J. R. Willis, On methods for bounding the overall properties of nonlinear composites, *J. Mech. Phys. Solids* 39 (1991) 73–86.
- [32] P. Ponte Castañeda, The effective mechanical properties of nonlinear isotropic composites, *J. Mech. Phys. Solids* 39 (1991) 45–71.
- [33] S. Torquato, Random Heterogeneous Media: Microstructure and Improved Bounds on Effective Properties, *Appl. Mech. Rev.* 44 (1991)

- 37–76.
- [34] P. Ponte Castañeda, G. DeBotton, G. Li, Effective properties of nonlinear inhomogeneous dielectrics, *Phys. Rev. B* 46 (1992) 4387–4394.
 - [35] S. Nemat-Nasser, N. Yu, M. Hori, Bounds and estimates of overall moduli of composites with periodic microstructure, *Mech. Mater.* 15 (1993) 163–181.
 - [36] B. Balendran, S. Nemat-Nasser, Bounds on elastic moduli of composites, *J. Mech. Phys. Solids* 43 (1995) 1825–1853.
 - [37] D. M. Kochmann, G. W. Milton, Rigorous bounds on the effective moduli of composites and inhomogeneous bodies with negative-stiffness phases, *J. Mech. Phys. Solids* 71 (2014) 46–63.
 - [38] S. Nemat-nasser, M. Hori, Universal Bounds for Overall Properties of Linear and Nonlinear Heterogeneous Solids, *Journal of Engineering Materials and Technology* 117 (2015) 412–432.
 - [39] B. Klusemann, H. Bohm, B. Svendsen, Homogenization methods for multi-phase elastic composites with non-elliptical reinforcements: Comparisons and benchmarks, *Eur. J. Mech. A/Solids* 34 (2012) 21–37.
 - [40] L. C. Brinson, W. G. Knauss, Finite Element Analysis of Multiphase Viscoelastic Solids, *J. Appl. Mech.* 59 (1992) 730–737.
 - [41] L. C. Brinson, W. S. Lin, Comparison of micromechanics methods for effective properties of multiphase viscoelastic composites, *Compos. Struct.* 41 (1998) 353–367.
 - [42] K. Terada, N. Kikuchi, A class of general algorithms for multi-scale analyses of heterogeneous media, *Comput. Methods Appl. Mech. Eng.* 190 (2001) 5427–5464.
 - [43] C. Miehe, A. Koch, Computational micro-to-macro transitions of discretized microstructures undergoing small strains, *Arch. Appl. Mech.* 72 (2002) 300–317.
 - [44] F. Feyel, A multilevel finite element method (FE2) to describe the response of highly non-linear structures using generalized continua, *Comput. Methods Appl. Mech. Eng.* 192 (2003) 3233–3244.
 - [45] N. Moës, M. Cloirec, P. Cartraud, J. F. Remacle, A computational approach to handle complex microstructure geometries, *Comput. Methods Appl. Mech. Eng.* 192 (2003) 3163–3177.
 - [46] I. Özdemir, W. A. M. Brekelmans, M. G. D. Geers, Computational homogenization for heat conduction in heterogeneous solids, *Int. J. Numer. Methods Eng.* 73 (2008) 185–204.
 - [47] F. Fritzen, M. Leuschner, Reduced basis hybrid computational homogenization based on a mixed incremental formulation, *Comput. Methods Appl. Mech. Eng.* 260 (2013) 143–154.
 - [48] A. Javili, G. Chatzigeorgiou, P. Steinmann, Computational homogenization in magneto-mechanics, *Int. J. Solids Struct.* 50 (2013) 4197–4216.
 - [49] D. M. Kochmann, G. N. Venturini, Homogenized mechanical properties of auxetic composite materials in finite-strain elasticity, *Smart Mater. Struct.* 22 (2013) 084004.
 - [50] R. Biswas, L. H. Poh, A micromorphic computational homogenization framework for heterogeneous materials, *J. Mech. Phys. Solids* 102 (2017) 187–208.
 - [51] F. Larsson, K. Runesson, F. Su, Variationally consistent computational homogenization of transient heat flow, *Int. J. Numer. Methods Eng.* 81 (2010) 1659–1686.
 - [52] F. Feyel, J. L. Chaboche, FE2 multiscale approach for modelling the elastoviscoplastic behaviour of long fibre SiC/Ti composite materials, *Comput. Methods Appl. Mech. Eng.* 183 (2000) 309–330.
 - [53] F. Fritzen, M. Leuschner, Nonlinear reduced order homogenization of materials including cohesive interfaces, *Comput. Mech.* 56 (2015) 131–151.
 - [54] E. Tikarrouchine, F. Praud, G. Chatzigeorgiou, B. Piotrowski, Y. Chemisky, F. Meraghni, Three-dimensional FE² method for the simulation

- of non-linear, rate-dependent response of composite structures, *Composite Structures* 193 (2018) 165–179.
- [55] G. Chatzigeorgiou, N. Charalambakis, Y. Chemisky, F. Meraghni, *Thermomechanical Behavior of Dissipative Composite Materials*, ISTE Press - Elsevier, London, 2018.
- [56] S. Saeb, P. Steinmann, A. Javili, Aspects of Computational Homogenization at Finite Deformations: A Unifying Review From Reuss' to Voigt's Bound, *Appl. Mech. Rev.* 68 (2016) 050801.
- [57] M. G. D. Geers, V. Kouznetsova, W. A. M. Brekelmans, Multi-scale computational homogenization: Trends and challenges, *J. Comput. Appl. Math.* 234 (2010) 2175–2182.
- [58] N. Charalambakis, G. Chatzigeorgiou, Y. Chemisky, F. Meraghni, Mathematical homogenization of inelastic dissipative materials: A survey and recent progress, *Continuum Mechanics and Thermodynamics* 30 (2018) 1–51.
- [59] S. Yadegari, S. Turteltaub, A. S. Suiker, Generalized grain cluster method for multiscale response of multiphase materials, *Comput. Mech.* 56 (2015) 193–219.
- [60] K. Matsui, K. Terada, K. Yuge, Two-scale finite element analysis of heterogeneous solids with periodic microstructures, *Comput. Struct.* 82 (2004) 593–606.
- [61] J. C. Michel, H. Moulinec, P. Suquet, Effective properties of composite materials with periodic microstructure: a computational approach, *Comput. Methods Appl. Mech. Eng.* 172 (1999) 109–143.
- [62] J. Yvonnet, E. Monteiro, Q. C. He, Computational homogenization method and reduced database model for hyperelastic heterogeneous structures, *Int. J. Multiscale Comput. Eng.* 11 (2013) 201–225.
- [63] B. Le, J. Yvonnet, Q. He, Computational homogenization of nonlinear elastic materials using neural networks, *Int. J. Numer. Methods Eng.* 104 (2015) 1061–1084.
- [64] P. M. Suquet, Local and global aspects in the mathematical theory of plasticity, *Plast. today* (1985) 279–309.
- [65] O. Pierard, C. Friebel, I. Doghri, Mean-field homogenization of multi-phase thermo-elastic composites: A general framework and its validation, *Compos. Sci. Technol.* 64 (2004) 1587–1603.
- [66] B. S. Mercer, K. K. Mandadapu, P. Papadopoulos, Novel formulations of microscopic boundary-value problems in continuous multiscale finite element methods, *Comput. Methods Appl. Mech. Eng.* 286 (2015) 268–292.
- [67] Z. Yuan, J. Fish, Toward realization of computational homogenization in practice, *Int. J. Numer. Methods Eng.* 73 (2008) 361–380.
- [68] V. D. Nguyen, E. Béchet, C. Geuzaine, L. Noels, Imposing periodic boundary condition on arbitrary meshes by polynomial interpolation, *Comput. Mater. Sci.* 55 (2012) 390–406.
- [69] S. Pecullan, L. V. Gibiansky, S. Torquato, Scale effects on the elastic behavior of periodic and hierarchical two-dimensional composites, *J. Mech. Phys. Solids* 47 (1999) 1509–1542.
- [70] S. Hazanov, C. Huet, Order relationships for boundary conditions effect in heterogeneous bodies smaller than the representative volume, *J. Mech. Phys. Solids* 42 (1994) 1995–2011.
- [71] S. Hazanov, M. Amieur, On overall properties of elastic heterogeneous bodies smaller than the representative volume, *Int. J. Eng. Sci.* 33 (1995) 1289–1301.
- [72] D. H. Pahr, P. K. Zysset, Influence of boundary conditions on computed apparent elastic properties of cancellous bone, *Biomech. Model. Mechanobiol.* 7 (2008) 463–476.
- [73] K. Terada, M. Hori, T. Kyoya, N. Kikuchi, Simulation of the multi-scale convergence in computational homogenization approaches, *Int. J. Solids Struct.* 37 (2000) 2285–2311.
- [74] X. Yuan, Y. Tomita, Effective Properties of Cosserat Composite With Periodic Microstructure, *Mech. Res. Commun.* 28 (2001) 265–270.
- [75] M. Jiang, K. Alzebedeh, I. Jasiuk, M. Ostoj-Starzewski, Scale and boundary conditions effects in elastic properties of random composites,

- Acta Mech. 148 (2001) 63–78.
- [76] M. Ostoja-Starzewski, Material spatial randomness: From statistical to representative volume element, *Probabilistic Eng. Mech.* 21 (2006) 112–132.
- [77] A. Drago, M. J. Pindera, Micro-macromechanical analysis of heterogeneous materials: Macroscopically homogeneous vs periodic microstructures, *Compos. Sci. Technol.* 67 (2007) 1243–1263.
- [78] S. Saroukhani, R. Vafadari, R. Andersson, F. Larsson, K. Runesson, On statistical strain and stress energy bounds from homogenization and virtual testing, *Eur. J. Mech. A/Solids* 51 (2015) 77–95.
- [79] V. D. Nguyen, L. Wu, L. Noels, Unified treatment of microscopic boundary conditions and efficient algorithms for estimating tangent operators of the homogenized behavior in the computational homogenization method, *Comput. Mech.* 59 (2017) 483–505.
- [80] I. M. Gitman, H. Askes, E. C. Aifantis, The representative volume size in static and dynamic micro-macro transitions, *Int. J. Fract.* 135 (2005) 3–9.
- [81] Z. F. Khisaeva, M. Ostoja-Starzewski, On the size of RVE in finite elasticity of random composites, *J. Elast.* 85 (2006) 153–173.
- [82] I. Temizer, T. I. Zohdi, A numerical method for homogenization in non-linear elasticity, *Comput. Mech.* 40 (2007) 281–298.
- [83] M. Thomas, N. Boyard, L. Perez, Y. Jarny, D. Delaunay, Representative volume element of anisotropic unidirectional carbon-epoxy composite with high-fibre volume fraction, *Compos. Sci. Technol.* 68 (2008) 3184–3192.
- [84] I. Temizer, T. Wu, P. Wriggers, On the optimality of the window method in computational homogenization, *Int. J. Eng. Sci.* 64 (2013) 66–73.
- [85] J. Dirrenberger, S. Forest, D. Jeulin, Towards gigantic RVE sizes for 3D stochastic fibrous networks, *Int. J. Solids Struct.* 51 (2014) 359–376.
- [86] J. Schröder, D. Balzani, D. Brands, Approximation of random microstructures by periodic statistically similar representative volume elements based on lineal-path functions, *Arch. Appl. Mech.* 81 (2011) 975–997.
- [87] D. Balzani, L. Scheunemann, D. Brands, J. Schröder, Construction of two- and three-dimensional statistically similar RVEs for coupled micro-macro simulations, *Comput. Mech.* 54 (2014) 1269–1284.
- [88] R. Glüge, M. Weber, A. Bertram, Comparison of spherical and cubical statistical volume elements with respect to convergence, anisotropy, and localization behavior, *Comput. Mater. Sci.* 63 (2012) 91–104.
- [89] C. Miehe, Computational micro-to-macro transitions for discretized micro-structures of heterogeneous materials at finite strains based on the minimization of averaged incremental energy, *Comput. Methods Appl. Mech. Eng.* 192 (2003) 559–591.
- [90] P. Kanouté, D. P. Boso, J. L. Chaboche, B. A. Schrefler, Multiscale methods for composites: A review, *Archives of Computational Methods in Engineering* 16 (2009) 31–75.
- [91] K. Matous, M. G. Geers, V. G. Kouznetsova, A. Gillman, A review of predictive nonlinear theories for multiscale modeling of heterogeneous materials, *Journal of Computational Physics* 330 (2017) 192–220.
- [92] V. Kouznetsova, W. A. M. Brekelmans, F. P. T. Baaijens, An approach to micro-macro modeling of heterogeneous materials, *Comput. Mech.* 27 (2001) 37–48.
- [93] P. Ladevèze, O. Loiseau, D. Dureisseix, A micro-macro and parallel computational strategy for highly heterogeneous structures, *Int. J. Numer. Methods Eng.* 52 (2001) 121–138.
- [94] C. Miehe, J. Dettmar, A framework for micro-macro transitions in periodic particle aggregates of granular materials, *Comput. Methods Appl. Mech. Eng.* 193 (2004) 225–256.
- [95] C. Stolz, On micro-macro transition in non-linear mechanics, *Materials (Basel)*. 3 (2010) 296–317.
- [96] Q. Liu, X. Liu, X. Li, S. Li, Micro-macro homogenization of granular materials based on the average-field theory of Cosserat continuum, *Adv. Powder Technol.* 25 (2014) 436–449.
- [97] G. Chatzigeorgiou, Y. Chemisky, F. Meraghni, Computational micro to macro transitions for shape memory alloy composites using periodic

1
2
3
4
5
6
7
8
9
10
11
12
13
14
15
16
17
18
19
20
21
22
23
24
25
26
27
28
29
30
31
32
33
34
35
36
37
38
39
40
41
42
43
44
45
46
47
48
49
50
51
52
53
54
55
56
57
58
59
60

homogenization, *Smart Mater. Struct.* 24 (2015) 035009.

[98] G. Chatzigeorgiou, F. Meraghni, A. Javili, Generalized interfacial energy and size effects in composites, *Journal of the Mechanics and Physics of Solids* 106 (2017) 257–282.

[99] F. Larsson, K. Runesson, S. Saroukhani, R. Vafadari, Computational homogenization based on a weak format of micro-periodicity for RVE-problems, *Comput. Methods Appl. Mech. Eng.* 200 (2011) 11–26.

[100] A. Javili, S. Saeb, P. Steinmann, Aspects of implementing constant traction boundary conditions in computational homogenization via semi-Dirichlet boundary conditions, *Comput. Mech.* 59 (2017) 21–35.

[101] Z. Hashin, On Elastic Materials Behaviour of Arbitrary of Fibre Reinforced Phase Transverse Geometry, *Journal of the Mechanics and Physics of Solids* 13 (1965) 119–134.

[102] L. J. Walpole, On bounds for the overall elastic moduli of inhomogeneous systems-I, *Journal of the Mechanics and Physics of Solids* 14 (1966) 151–162.

[103] G. J. Weng, Explicit evaluation of Willis’ bounds with ellipsoidal inclusions, *International Journal of Engineering Science* 30 (1992) 83–92.

[104] Z. Hashin, Analysis of Composite Materials-A survey, *Journal of Applied Mechanics* 50 (1983) 481–505.

[105] D. Savvas, G. Stefanou, M. Papadrakakis, G. Deodatis, Homogenization of random heterogeneous media with inclusions of arbitrary shape modeled by XFEM, *Comput. Mech.* 54 (2014) 1221–1235.

[106] S. Ghosh, K. Lee, S. Moorthy, Multiple scale analysis of heterogeneous elastic structures using homogenization theory and voronoi cell finite element method, *Int. J. Solids Struct.* 32 (1995) 27–62.